

Schrödinger cat states of a nuclear spin qudit in silicon

Received: 18 April 2024

Accepted: 26 November 2024

Published online: 14 January 2025

 Check for updates

Xi Yu¹, Benjamin Wilhelm¹, Danielle Holmes¹, Arjen Vaartjes¹, Daniel Schwienbacher¹, Martin Nurizzo¹, Anders Kringhøj¹, Mark R. van Blankenstein¹, Alexander M. Jakob^{1,2,3}, Pragati Gupta^{1,4}, Fay E. Hudson^{1,5}, Kohei M. Itoh^{1,6}, Riley J. Murray⁷, Robin Blume-Kohout^{1,7}, Thaddeus D. Ladd⁸, Namit Anand^{1,9,10}, Andrew S. Dzurak^{1,5}, Barry C. Sanders^{1,4}, David N. Jamieson^{1,2,3} & Andrea Morello¹✉

High-dimensional quantum systems are a valuable resource for quantum information processing. They can be used to encode error-correctable logical qubits, which has been demonstrated using continuous-variable states in microwave cavities or the motional modes of trapped ions. For example, high-dimensional systems can be used to realize ‘Schrödinger cat’ states, which are superpositions of widely displaced coherent states that can be used to illustrate quantum effects at large scales. Recent proposals have suggested encoding qubits in high-spin atomic nuclei, which are finite-dimensional systems that can host hardware-efficient versions of continuous-variable codes. Here we demonstrate the creation and manipulation of Schrödinger cat states using the spin-7/2 nucleus of an antimony atom embedded in a silicon nanoelectronic device. We use a multi-frequency control scheme to produce spin rotations that preserve the symmetry of the qudit, and we constitute logical Pauli operations for qubits encoded in the Schrödinger cat states. Our work demonstrates the ability to prepare and control non-classical resource states, which is a prerequisite for applications in quantum information processing and quantum error correction, using our scalable, manufacturable semiconductor platform.

A spin-1/2 particle is the textbook example of a physical object used to encode one qubit (Hilbert space dimension $d = 2$) in a discrete-variable paradigm. The ‘quantumness’ of spin has been recognized since the Stern-Gerlach experiment but is otherwise surprisingly elusive. The dynamics for spin-1/2 maps directly to the precession of a classical gyroscope¹, and its statistics can be cast within local hidden-variable models². Entangling several qubits to obtain a $d \gg 2$ -dimensional Hilbert space is, therefore, essential for capturing the true power of quantum information.

At the other extreme, continuous-variable quantum computing encodes information in the intrinsically $d \rightarrow \infty$ dimensional Hilbert space of a quantum harmonic oscillator^{3–6}. The state of the system is described by the complex quadratures of a bosonic field, and the ‘quantumness’ of the encoded states becomes rather transparent. Classical fields have a Gaussian-shaped distribution in the complex plane, whereas quantum resource states have non-Gaussian statistics⁷. A famous example is the Schrödinger cat state, a superposition of

¹School of Electrical Engineering and Telecommunications, UNSW Sydney, Sydney, New South Wales, Australia. ²Centre for Quantum Computation and Communication Technology, Melbourne, Victoria, Australia. ³School of Physics, University of Melbourne, Melbourne, Victoria, Australia. ⁴Institute for Quantum Science and Technology, University of Calgary, Calgary, Alberta, Canada. ⁵Diraq Pty. Ltd, Sydney, New South Wales, Australia. ⁶School of Fundamental Science and Technology, Keio University, Kohoku-ku, Yokohama, Japan. ⁷Quantum Performance Laboratory, Sandia National Laboratories, Albuquerque, NM, USA. ⁸HRL Laboratories, LLC, Malibu, CA, USA. ⁹Quantum Artificial Intelligence Laboratory (QuAIL), NASA Ames Research Center, Moffett Field, CA, USA. ¹⁰KBR, Inc., Houston, TX, USA. ✉e-mail: a.morello@unsw.edu.au

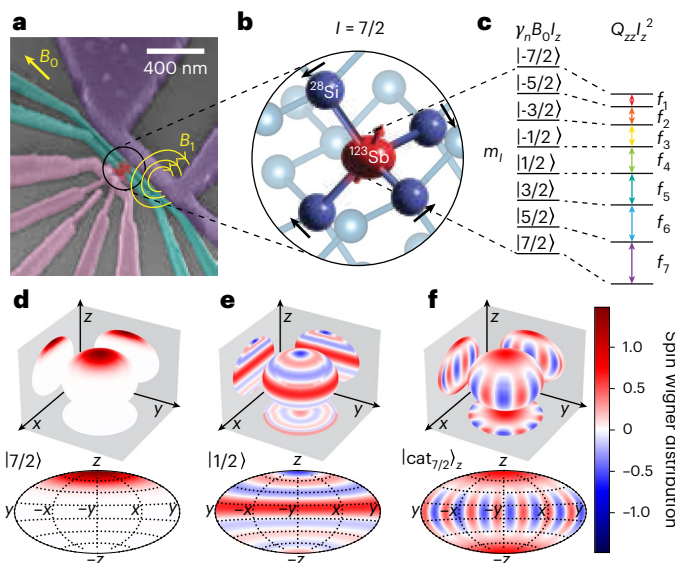


Fig. 1 | The eight-dimensional ^{123}Sb nuclear spin qudit in silicon. **a**, False-colour scanning electron micrograph of a characteristic silicon device showing the single electron transistor (pink), gates for tuning the electric potential of the donor (green), microwave antenna (purple) and donor implant window (red). The donor is subject to an oscillating magnetic field B_1 from the microwave antenna, which is perpendicular to an in-plane external field $B_0 = 1.384 \text{ T}$. **b**, The ^{123}Sb donor in the ^{28}Si crystal lattice. Black arrows illustrate the shear strain on Si atoms bonded to ^{123}Sb , which creates an electric field gradient, resulting in a nuclear quadrupole shift. **c**, Energy levels of the ionized ^{123}Sb donor. The Zeeman energy $\gamma_n B_0 \hat{l}_z$ produces equispaced nuclear energy levels, whereas the quadrupole coupling, here in the simplified form $Q_{zz} \hat{l}_z^2$, shifts the energy levels depending on the spin projection m_l , resulting in seven individually addressable NMR transitions, labelled by the coloured arrows. **d–f**, Theoretical spin Wigner function on a sphere (top) ^{44,45} and corresponding Hammer projections (bottom) for the example states: $|7/2\rangle$ (**d**) and $|1/2\rangle$ (**e**) spin projection eigenstates and the $|\text{cat}_{7/2}\rangle_z$ Schrödinger cat state (**f**). The grey planes in the Wigner plots show the mirrored reflections of the sphere. The colour bar for the Wigner function shown here is used without rescaling throughout the rest of this work.

two coherent states far displaced from each other^{8–10}. Its quantumness is captured by the negativity of the Wigner function¹¹, which also implies contextuality and, for multi-particle systems with spatial extent, non-locality. The key to creating non-classical states is always nonlinearity, without which it would be possible to displace only trivial Gaussian states.

The intermediate regime, comprising qudits with $3 \leq d < \infty$, is very rich^{12–16} but relatively unexplored. Once $d \geq 3$, it becomes possible to create states that violate local-hidden-variable theories² and to encode error-correctable logical qubits within a single quantum object^{17–19}, without resorting to entangling several physical qubits.

In this work, we experimentally demonstrate the creation and manipulation of Schrödinger cat states of a single antimony-123 (^{123}Sb) nuclear spin qudit in silicon^{20,21}. The $I = 7/2$ nuclear spin of ^{123}Sb results in a $d = 2I + 1 = 8$ dimensional Hilbert space. Although eight is not infinity, it is large enough to accommodate non-trivial quantum states with properties notably like those of bosonic states in continuous-variable systems (see Supplementary Information Section 1 for an introduction to spin coherent states and Supplementary Information Section 2 for a review of the spin Wigner function in finite-dimensional systems). Crucially, it is enough to support a logical qubit encoding capable of correcting all first-order rotation errors¹⁷.

SU(8) and SU(2) operations in a generalized rotating frame

The device structure follows that of early experiments on single donors in silicon (Fig. 1a). During the quantum operations, the ^{123}Sb

donor is kept in the ionized, charge-positive D^+ state. In the absence of a hyperfine-coupled electron, the nuclear spin Hamiltonian (in frequency units) takes the form:

$$\hat{\mathcal{H}}_{\text{D}^+} = -\gamma_n B_0 \hat{l}_z + \sum_{\alpha, \beta \in \{x, y, z\}} Q_{\alpha\beta} \hat{l}_\alpha \hat{l}_\beta, \quad (1)$$

where $B_0 = 1.384 \text{ T}$ is a static magnetic field, $\gamma_n = 5.55 \text{ MHz T}^{-1}$ is the nuclear gyromagnetic ratio, $\alpha, \beta = \{x, y, z\}$ are Cartesian axes, \hat{l}_α are the eight-dimensional nuclear spin operators and $Q_{\alpha\beta}$ is the interaction energy between the electric quadrupole moment of the nucleus and an electric field gradient, which arises mostly from local strain breaking the cubic symmetry of the silicon lattice²⁰ (Fig. 1b).

The electric quadrupole interaction is a nonlinear term that enables universal control of the antimony qudit. Although the Zeeman interaction, a linear function of the \hat{l}_z operator, splits the energies of the nuclear spin eigenstates $|l, m_l\rangle$, $m_l = -l, -l+1, \dots, l$, uniformly by $f_0^+ = \gamma_n B_0 \approx 7.7 \text{ MHz}$ (the superscript + labels quantities pertaining to the ionized D^+ donor state), the quadrupole term introduces a non-uniform spacing, so that the nuclear magnetic resonance (NMR) frequencies between pairs of eigenstates differ by $f_q^+ \approx 28 \text{ kHz}$ (Fig. 1c). As $f_0^+ \gg f_q^+$, the eigenstates of $\hat{\mathcal{H}}_{\text{D}^+}$ are simply the $|m_l\rangle$ eigenstates of \hat{l}_z (in the following, we drop the spin quantum number l from the notation, as it is always $7/2$). Notably, only the $|\pm 7/2\rangle$ states (Fig. 1d) are spin coherent states. All other eigenstates of \hat{l}_z have non-Gaussian Wigner functions that display strong negativity (Fig. 1e,f).

This energy level structure allows for universal control of the spin qudit²¹ by applying a NMR control Hamiltonian of the form:

$$\hat{\mathcal{H}}_1(t) = -\gamma_n \hat{l}_x \sum_{k=1}^{2I} \cos(2\pi f_k t + \phi_k) B_{1,k}(t), \quad (2)$$

where f_k are the NMR frequencies ($f_1 = \langle -7/2 | \hat{\mathcal{H}}_{\text{D}^+} | -7/2 \rangle - \langle -5/2 | \hat{\mathcal{H}}_{\text{D}^+} | -5/2 \rangle$ and so on), $B_{1,k}(t)$ the oscillating magnetic field amplitudes and ϕ_k the phases. Universal $SU(8)$ control requires $d^2 - 1 = 63$ parameters, but we can exploit the ability to prepare the spin in one of the Hamiltonian eigenstates, which guarantees that the $(d-1)^2 = 49$ $U(7)$ operations on the other seven eigenstates have no effect, thus reducing the required number of parameters to 14. These are provided by the seven amplitudes $B_{1,k}(t)$ and seven phases ϕ_k . The time-dependence of the pulses allows universal control for generating any $SU(d)$ unitary in $\mathcal{O}(d^2)$ steps^{22,23}. We produced $\hat{\mathcal{H}}_1(t)$ by direct digital synthesis with a field-programmable gate array (FPGA) waveform generator. Crucially, the generator software creates seven ‘virtual clocks’ that allow us to define a generalized rotating frame²⁴ (GRF; Supplementary Information Section 4) wherein the spin state appears static in the absence of drives. In other words, the GRF cancels all terms of the static Hamiltonian, whereas a single-frequency frame would cancel only terms proportional to \hat{l}_z . The phases ϕ_k of the virtual clocks can be shifted by software instructions alone, allowing the establishment of arbitrary relative phases between the eight levels, corresponding to \hat{l}_z rotations, \hat{l}_x rotations and in fact any diagonal unitary, whereas a single-frequency rotating frame and frame shifting would only enact \hat{l}_z control.

Within the GRF, we demonstrate a covariant rotation²⁵ of the large spin, that is an $SU(2)$ rotation where the spin state is rigidly rotated around an axis of the Bloch sphere, thus preserving the shape of the Wigner function. This is important because the $SU(2)$ covariant rotation is the native logical operation on logical qubits encoded in the eight-dimensional Hilbert space of the nucleus^{17,18}. We first prepared the spin in the $|-7/2\rangle$ eigenstate (see Supplementary Information Section 11 for the spin initialization), then simultaneously applied seven tones at $\{f_k\}$, all with the same amplitude (22.86 mV for each tone), resulting in equal magnetic field amplitudes $B_{1,k}(t) = B_1(t)$ for all k . As the tones were applied exactly on resonance with each f_k , the rotations were always around an axis placed on the equator of the GRF, denoted

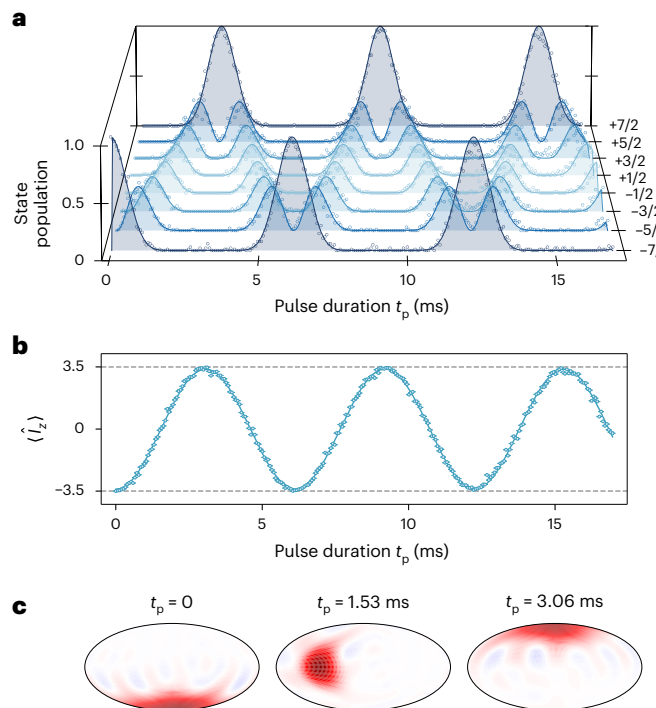


Fig. 2 | Covariant SU(2) rotations. **a**, Population of the $|m_l\rangle$ states as a function of duration t_p of an NMR pulse of seven tones with equal amplitude. The pulse drives a covariant SU(2) rotation of an initial $|{-7/2}\rangle$ spin coherent state. Solid lines are calculations (not fits) assuming perfect initialization and control. Here and elsewhere, data points are raw values, with no post-selection or state preparation and measurement error extraction. The population of each nuclear spin state was measured over 100 repetitions. **b**, Expectation value of \hat{l}_z as a function of pulse duration, calculated from the data in **a**. **c**, Wigner function of reconstructed states with rotation angle $\theta = 0, \pi/2$ and π at the times indicated by t_p , showing that the Wigner distribution is rotated rigidly around the $-y$ axis.

by a single longitude φ . Calling θ the rotation angle, we denote such operations with $R_\theta(\varphi)$. Monitoring the populations of the $|m_l\rangle$ eigenstates as a function of pulse duration, that is θ (Fig. 2a), we found the predicted behaviour for a spin undergoing a rotation around the $-y$ axis of the $I = 7/2$ Bloch sphere. Calculating the $\langle \hat{l}_z \rangle$ expectation value revealed the expected behaviour of a covariant Rabi oscillation of the large spin (Fig. 2b), with Rabi frequency $f_{\text{Rabi}}^{\text{CR}} = 163.4(1)$ Hz. Here and elsewhere, error bars represent 1σ confidence intervals. Snapshots of the spin Wigner function (see Supplementary Information Section 2 for the spin Wigner function and Supplementary Information Section 9 for density matrix reconstruction) at different times confirm the picture of a smoothly evolving spin coherent state, which preserves its shape as it rotates (Fig. 2c). The experiment was conducted in the $\gamma_B B_1 \ll f_q^+$ regime (see Supplementary Information Section 4C for a discussion of the general case), where the power broadening was negligible compared to the spacing between the NMR resonances, making it sufficient to adopt simple rectangular $B_1(t)$ pulse envelopes.

Generation and manipulation of Schrödinger cat states

With $SU(8)$ and $SU(2)$ rotations available, we proceeded to generate the z -oriented Schrödinger cat state of the high-spin nucleus, $|\text{cat}_{7/2}\rangle_z = (|7/2\rangle + e^{i\xi_7} |{-7/2}\rangle)/\sqrt{2}$ (ξ_k denotes the relative phase between the branches of the superposition of $|\pm k/2\rangle$ states) using two different methods (Fig. 1f). The first, based on Givens rotations²⁶, simply involves preparing the $|{-7/2}\rangle$ state, applying a $\pi/2$ pulse at f_1 to produce $(|{-7/2}\rangle - |{-5/2}\rangle)/\sqrt{2}$ and then applying a sequence of π pulses between ascending pairs of states (Fig. 3a,b). The quality of the resulting $|\text{cat}_{7/2}\rangle_z$ state was assessed by measuring the contrast C_p of the parity oscillations around the equator of the Bloch sphere (Fig. 3c).

For this, we applied covariant rotations $R_{\pi/2}(\varphi)$ around different axes in the GRF, indexed by the longitude φ , and then measured the expectation value of the parity operator $\hat{P} = \sum_{m_l} (-1)^{l+m_l} |m_l\rangle \langle m_l|$ of the resulting states. The parity oscillations displayed a contrast $C_p = 0.878(3)$, which we extracted with a sinusoidal fit $\langle \hat{P}(\varphi) \rangle \propto C_p \sin(7\varphi)$ (see Supplementary Information Section 8 for details of the parity measurement). We plotted the Wigner function (Fig. 3d) from the reconstructed density matrix ρ_{MLE} , which was obtained from maximum-likelihood-estimation quantum state tomography (Supplementary Information Section 9). The Wigner function reveals the increasing number of interference fringes at each step of the process, from 0 in the $|{-7/2}\rangle$ state to seven in the $|\text{cat}_{7/2}\rangle_z$ state. From the reconstructed density matrix ρ_{MLE} , we calculated the state fidelity $\mathcal{F} = \langle \psi | \rho_{\text{MLE}} | \psi \rangle = 0.794(2)$, where $|\psi\rangle = |\text{cat}_{7/2}\rangle_z = (|7/2\rangle + e^{i\xi_7} |{-7/2}\rangle)/\sqrt{2}$ is the target state, with $\xi_7 = \pi$. Unlike the contrast of the parity oscillation, the state fidelity depended sensitively on the phase of the state relative to the target. The state reconstruction revealed a systematic phase shift $\Delta\xi_7 = +39.3^\circ$, which could, in principle, be cancelled by a redefinition of the GRF (see below). Removing the phase shift resulted in $\mathcal{F} = 0.884(2)$ for this cat state.²⁷

An alternative method for generating the $|\text{cat}_{7/2}\rangle_z$ state²⁷ makes explicit use of the software-defined GRF. Starting from $|{-7/2}\rangle$, we applied a $\pi/2$ covariant $SU(2)$ rotation to prepare a coherent state on the equator of the Bloch sphere. We then sent an instruction to the FPGA to redefine the phases ϕ_k of the GRF, thus shifting the odd clocks ($f_{1,3,5,7}$) by -90° and the even ones ($f_{2,4,6}$) by $+90^\circ$. This embodied one-axis twisting dynamics²⁷, instantly and error-free (to within the time resolution of the FPGA, 4 ns). In the redefined GRF, the state of the spin was now the x -oriented cat state $|\text{cat}_{7/2}\rangle_x$ (Supplementary Information Section 6). We call this operation a ‘virtual SNAP’, as it is mathematically analogous to the selective number-dependent arbitrary phase (SNAP) operation, first introduced in microwave cavities coupled to superconducting qubits²⁸. In contrast to the linear cavity system, our system does not require an ancilla qubit to achieve state-selective phase shifts, because it possesses an intrinsic nonlinearity, in the form of a quadrupole splitting, that permits state-selective operations. The operation is virtual because no physical action is applied to the system; it can be viewed as the multilevel extension of a virtual Z gate²⁹.

From the $|\text{cat}_{7/2}\rangle_x$, a further $SU(2)\pi/2$ rotation creates the cat state $|\text{cat}_{7/2}, \xi_7 = \pi/2\rangle_z = (|7/2\rangle + i|{-7/2}\rangle)/\sqrt{2}$. The cat state produced by virtual SNAP achieves a contrast of the parity oscillations $C_p = 0.982(5)$ and a state fidelity $\mathcal{F} = 0.874(2)$ from the reconstructed density matrix. Extracting the $\Delta\xi_7 = +24.1^\circ$ phase shift between the created cat and the target yields $\mathcal{F} = 0.913(2)$. The method of producing cat states by virtual SNAP plus covariant $SU(2)$ rotations is a key feature of our work and appears to yield superior fidelity compared to the Givens rotation method.

Cat states can be defined in subspaces other than $m_l = \pm 7/2$. For this purpose, we initialized the spin in the $|{-5/2}\rangle$, $|{-3/2}\rangle$ or $|{-1/2}\rangle$ states and then used the Givens rotations method to prepare $|\text{cat}_{5/2}\rangle_z = (|5/2\rangle + e^{i\xi_5} |{-5/2}\rangle)/\sqrt{2}$, $|\text{cat}_{3/2}\rangle_z = (|3/2\rangle + e^{i\xi_3} |{-3/2}\rangle)/\sqrt{2}$ and the trivial (that is, non-cat) state $(|1/2\rangle + e^{i\xi_1} |{-1/2}\rangle)/\sqrt{2}$. However, in these subspaces, it is no longer true that a multi-frequency drive all with the same amplitudes results in a covariant $SU(2)$ rotation, so the values of $B_{1,k}$ must be individually calibrated (see Supplementary Information Section 7 for details).

Coherence times

The multilevel control methods described above represent a promising new direction in quantum information processing. Furthermore, applying them to nuclear spins in isotopically enriched ^{29}Si gives access to a platform with exceptionally long coherence times^{30,31}. For single ^{123}Sb nuclei, the only data existing to date quantify the coherence of superpositions of two spin projection states with $\Delta m_l = 1$ or 2 (refs. 20,21). Here we report the coherence times of spin coherent and Schrödinger cat states. Figure 4a shows the results of a ‘covariant

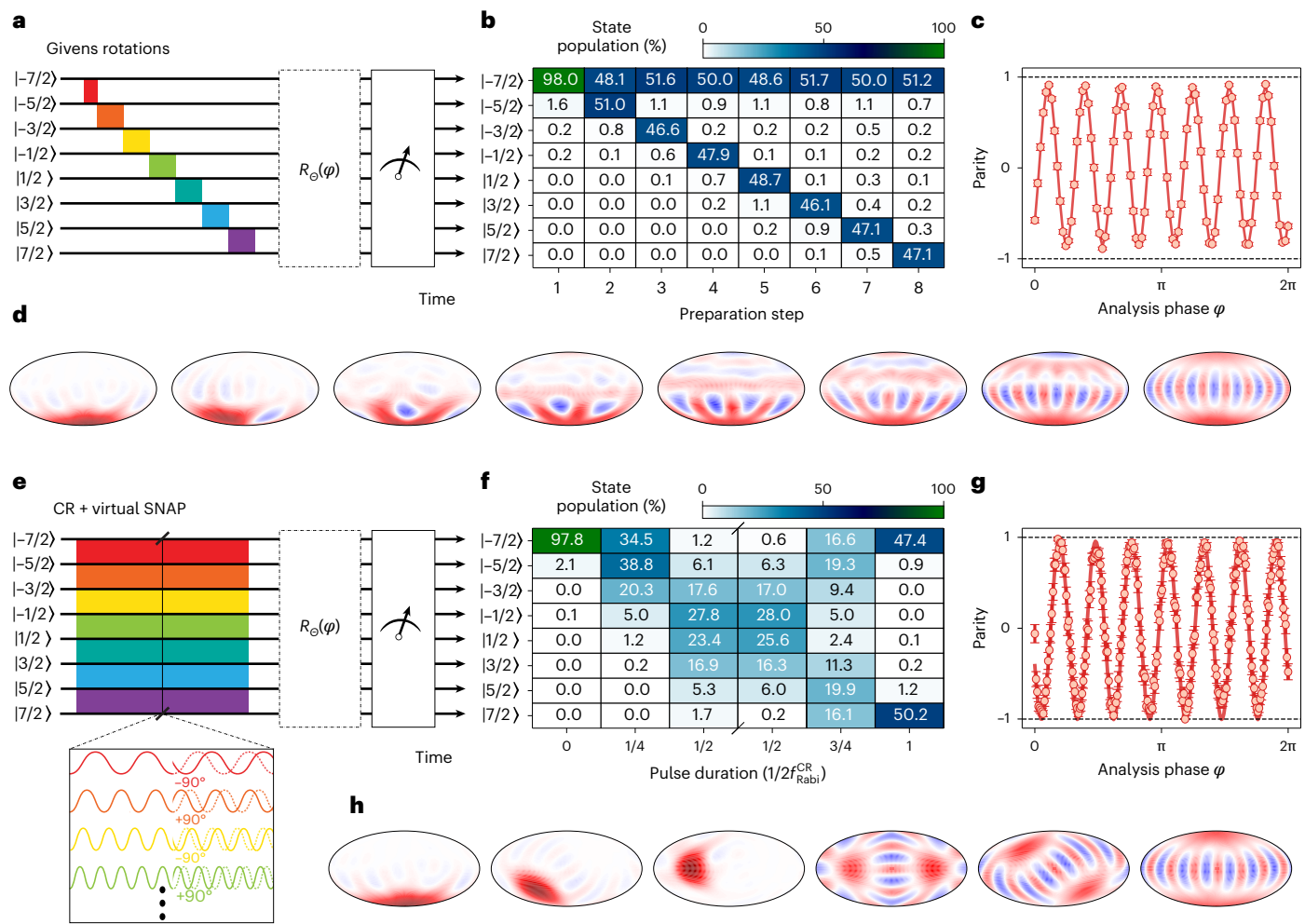


Fig. 3 | Creation of Schrödinger cat states. **a**, Pulse sequence for creating a cat state through Givens rotations. This is followed by a covariant $SU(2)$ rotation $R_\theta(\varphi)$ for tomography and measurement of the nuclear state populations. **b**, State populations at each step. **c**, Parity of the state after the tomography rotation pulse $R_{\pi/2}(\varphi)$, displaying the expected seven periods of oscillation, and a contrast $C_p = 0.878(3)$ of the cat state $|\text{cat}_{7/2}, \xi_7 = \pi/2\rangle_z = (|7/2\rangle - |{-7/2}\rangle)/\sqrt{2}$. Each parity was measured over 750 repetitions. Error bars are smaller than the symbol size. **d**, Reconstructed Wigner functions at each step. Note the increasing number of interference fringes. **e**, Pulse sequence for creating a cat state through

covariant $SU(2)$ rotations and virtual SNAP, which was implemented by shifting the phases of the GRF, as per the diagram below. **f**, State populations at the indicated steps along the protocol. **g**, Parity of the state after the tomography rotation pulse $R_{\pi/2}(\varphi)$, displaying seven periods of oscillations and a contrast $C_p = 0.982(5)$ of the cat state $|\text{cat}_{7/2}, \xi_7 = \pi/2\rangle_z = (|7/2\rangle + i|{-7/2}\rangle)/\sqrt{2}$. Each parity was measured over 100 repetitions. **h**, Reconstructed Wigner functions at the indicated steps. Note the instantaneous transition from a $-x$ -oriented coherent state to a cat state, caused by the virtual SNAP.

Ramsey' experiment in which we applied a covariant $SU(2)$ $\pi/2$ rotation around $-y$ in the GRF, waited a variable time τ and then applied a second covariant $SU(2)$ $\pi/2$ rotation around an equatorial axis, which shifted from $-y$ by a phase that increased with τ . This allowed us to observe fringes in $\langle \hat{I}_z \rangle(\tau)$ (the pulses were applied exactly on resonance). We fitted the observed fringes with a decaying sinusoid of the form $\langle \hat{I}_z \rangle(\tau) \propto 3.5 \exp[-(\tau/T_2^*)^{\alpha_R}]$, where $T_2^* = 49(2)$ ms is the dephasing time and $\alpha_R = 0.84(4)$ is the exponent of the Ramsey decay. A covariant Hahn echo was obtained by adding a covariant $SU(2)$ π pulse in the middle of the sequence (Fig. 4b). The extracted coherence time of the Hahn echo (found by fitting a decay with the same form as the Ramsey fringes) was $T_2^H = 114(5)$ ms, with decay exponent $\alpha_H = 0.61(3)$. The values of $\alpha_{R,H} < 1$ indicate stretched exponential decays, consistent with the spin coherent state prepared by the first covariant $SU(2)$ $\pi/2$ pulse being a Gaussian-like superposition of all $|m_I\rangle$ eigenstates and with the coherence between pairs of such states varies substantially depending on m_I (Supplementary Information Section 10).

For the Schrödinger cat states, we measured the contrast C_p of the parity oscillations while adding a wait time τ between preparation and

measurement (Fig. 4c). For the $|\text{cat}_{7/2}\rangle_z$ state, we found the dephasing time $T_2^* = 15.0(6)$ ms. Smaller cat states ($|\text{cat}_{5/2}\rangle_z$ and $|\text{cat}_{3/2}\rangle_z$) and the trivial $(|1/2\rangle + |{-1/2}\rangle)/\sqrt{2}$ state exhibited longer coherence (Fig. 4e), reflecting the smaller energy difference between the $|m_I\rangle$ states involved in the superposition. x -oriented cat states, here prepared with the virtual-SNAP method (Methods), exhibited longer coherence times than z -oriented ones and a weaker dependence on cat size. This is consistent with the smaller population of large $|m_I\rangle$ eigenstates in x cats; most of the weight was in the $|\pm 1/2\rangle$ states, which have the longest coherence time due to the first-order insensitivity to electrical noise (Supplementary Information Section 10).

We, thus, found that, like bosonic cat states in cavities, larger cat states dephase faster. For bosonic cats, this drawback is compensated by the exponential suppression of photon loss¹⁰, which is the key error mechanism there. In our case instead, the energy loss was completely negligible (the nuclear T_1 was effectively infinite), but there is still an advantage in using larger cat states, as they allow a larger number of phase-flip errors to be corrected (one for $|\text{cat}_{3/2}\rangle$, two for $|\text{cat}_{5/2}\rangle$ and three for $|\text{cat}_{7/2}\rangle$) when used as logical qubit encodings¹⁸.

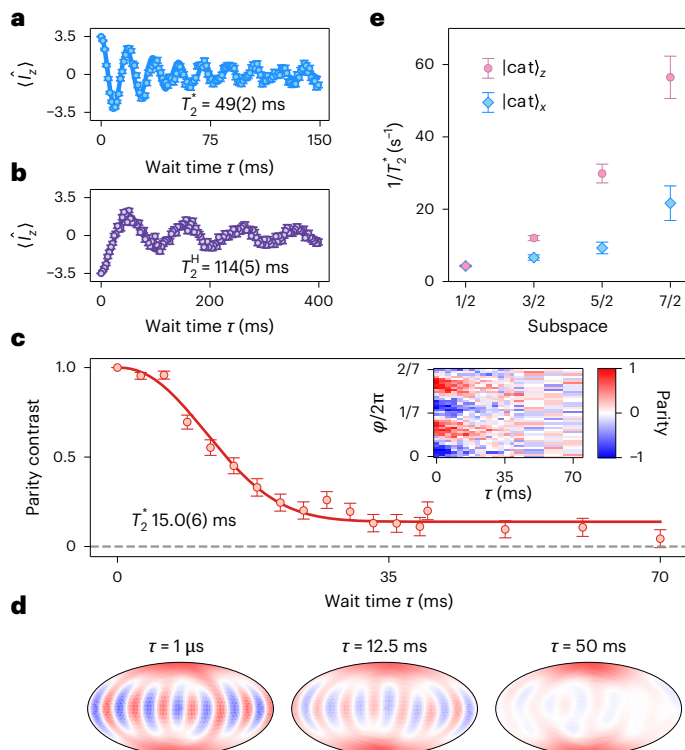


Fig. 4 | Dephasing of spin coherent states and Schrödinger cat states. **a**, Decay of Ramsey fringes for a spin coherent state prepared with a $SU(2)\pi/2$ pulse starting from $| -7/2 \rangle$, left to freely evolve for time τ and then rotated with a second $SU(2)\pi/2$ pulse around an angle φ increasing with τ . The dephasing time was $T_2^* = 49(2)$ ms. **b**, Hahn echo experiment, which had another $SU(2)\pi/2$ pulse at the halfway point, yielding coherence time $T_2^H = 114(5)$ ms. Each \hat{l}_z expectation in **a** and **b** was calculated from the probabilities of all eight nuclear spin states, each measured over 100 repetitions. **c**, Decay of the parity oscillations of a $|\text{cat}_{7/2}\rangle_z$ state with wait time, extracted from the data in the inset. Each parity measurement was an average over 50 repetitions. The cat state was prepared by the virtual-SNAP method and had coherence time $T_2^* = 15.0(6)$ ms. **d**, Reconstructed Wigner functions of an initial $|\text{cat}_{7/2}\rangle_z$ after the indicated wait times. Note the disappearance of interference fringes around the equator at long times. **e**, Dephasing rates for z cats (circles) and x cats (diamonds) as a function of subspace size. The dephasing rate was extracted from fitting the decay of the return probability, each averaged over 80 repetitions of spin projection measurements. The subspace cats $|\text{cat}\rangle_x$ were prepared by the virtual-SNAP method and $|\text{cat}\rangle_z$ by Givens rotations (Methods). Note that the x and z states in the $m_l = 1/2$ subspace coincide.

Outlook for quantum information processing

In this work, we have demonstrated a complete experimental toolbox for exploiting the eight-dimensional Hilbert space of a ^{123}Sb nucleus. The covariant $SU(2)$ rotations and the virtual-SNAP gates enable universal coherent control of a single qudit in any dimension (see Supplementary Information Section 5 for an explicit proof). This highlights the native universal capabilities of our device for high-dimensional and high-fidelity control. Although the dimensionality may lead one to think that a $I = 7/2$ nucleus is equivalent to $\log_2(2I+1) = 3$ qubits, a $|\text{cat}_{7/2}\rangle$ state on the nucleus is as macroscopic as a Greenberger–Horne–Zeilinger state on $2I = 7$ spin-1/2 qubits and maximizes the quantum Fisher information criterion for spins³². Another way to appreciate this point is to observe that the $2I + 1$ $|l, m_l\rangle$ eigenstates can be mapped onto the Dicke states of $2I$ spin-1/2 particles by a process known as a Dicke bootstrap³³, that is $|l, m_l\rangle \mapsto |D_{l-m_l}^{2I}\rangle$,

$$|D_{l-m_l}^{2I}\rangle = \frac{1}{\sqrt{\binom{2I}{l-m_l}}} \sum_{\sigma} \sigma |00\dots0\rangle_{l+m_l} |11\dots1\rangle_{l-m_l} \quad (3)$$

where σ denotes permutations over $2I$ qubits. A recent proposal¹⁸ makes use of the extreme bias in the physical noise affecting nuclear spin systems, $T_1 \gg T_2$, to encode a logical qubit in $|\text{cat}\rangle_x$ states. The spin-cat code for $I = 7/2$ can correct up to three phase-flip errors (see Supplementary Information Section 3 for the Schrödinger cat encoding). This would be surprising if one thought of the spin-7/2 state as a three-qubit equivalent, as a three-qubit repetition code can correct only one phase flip, but understandable if one considers the spin-7/2 cat state to be the equivalent of a seven-qubit code. Here, we have demonstrated the preparation of $|\text{cat}_{7/2}\rangle_x$ states that manifest the biased-noise encoding and the manipulation of cat states with $SU(2)$ rotations, which have bias-preserving logical Pauli operations. We verified that the nuclear relaxation time is extremely long, $T_1 \gg 1\ \text{s}$ (Supplementary Fig. 17), thus confirming that the biased-noise model is accurate.

Another proposal by Gross¹⁷ showed that it is possible to encode in a large spin a logical qubit that satisfies the Knill–Laflamme error correction conditions³⁴ for first-order $SU(2)$ errors. The minimum spin size required for a code that corrects all rotation errors ($|\hat{l}_x, \hat{l}_y, \hat{l}_z\rangle$) is $I = 7/2$ (ref. 17). Thus, a ^{123}Sb nucleus can also encode a qubit to protect information from unbiased depolarizing noise on a single spin. After encoding, a basis transformation from the error states to the energy eigenbasis converts rotation errors into populations of $|l, m_l < l\rangle$ eigenstates, which can be measured to detect the occurrence of the error³⁵. Crucially, the Gross code has $SU(2)$ rotations as the native logical gates on the encoded qubit. Therefore, our work provides a demonstration of such logical gates.

Our work brings high-dimensional quantum information processing and logical qubit encoding to the realm of atomic-scale semiconductor devices. In the near term, multi-qubit logic gates can be realized if two or more ^{123}Sb nuclei are hyperfine-coupled to a common electron. This would permit the implementation of a geometric CZ gate by imparting a 2π rotation to the electron, conditional on some specific state or states of the two nuclei³⁶. The fabrication of tightly spaced (~5 nm) ^{123}Sb donors could be made near-deterministic by implanting Sb_2^+ molecular ions³⁷. In the medium term, ion-implanted donors³⁸ could be naturally integrated with lithographic quantum dots, which serve as a reservoir for ancillae in repeated rounds of error detection and correction. A dot-mediated single-spin-qudit system holds the promise of achieving beyond-break-even logical qubit lifetimes and fault-tolerant operations. Accounting for control and read-out devices and assuming medium-range coupling, for example, by an electric dipole interaction³⁹ or through intermediary quantum dots⁴⁰, one ^{123}Sb qudit could occupy a footprint of order $200 \times 200\ \text{nm}^2$, affording, in principle, up to 25,000,000 logical qubits in a square millimetre. The technological challenges in building such a device remain formidable, but the formation of deterministic donor arrays by ion implantation is well underway³⁷, and the technology is compatible with industry-standard metal–oxide–semiconductor processes, which are being adapted to the development of quantum hardware⁴¹.

During the preparation of this manuscript we became aware of related work in which synthetic spin-7/2 equivalents were formed using the eight-dimensional Hilbert space of a transmon qudit⁴² and a superconducting harmonic oscillator⁴³, and $SU(2)$ operations and Schrödinger cat states were similarly demonstrated. These results highlight the maturity and universality of high-dimensional quantum computing, and its readiness to underpin logical qubit platforms.

Online content

Any methods, additional references, Nature Portfolio reporting summaries, source data, extended data, supplementary information, acknowledgements, peer review information; details of author contributions and competing interests; and statements of data and code availability are available at <https://doi.org/10.1038/s41567-024-02745-0>.

References

1. Slichter, C. P. *Principles of Magnetic Resonance*, Vol. 1 (Springer Science & Business Media, 2013).
2. Kochen, S. & Specker, E. The problem of hidden variables in quantum mechanics. *J. Math. Mech.* **17**, 59 (1967).
3. Gottesman, D., Kitaev, A. & Preskill, J. Encoding a qubit in an oscillator. *Phys. Rev. A* **64**, 012310 (2001).
4. Braunstein, S. L. & Van Loock, P. Quantum information with continuous variables. *Rev. Mod. Phys.* **77**, 513 (2005).
5. Flühmann, C. et al. Encoding a qubit in a trapped-ion mechanical oscillator. *Nature* **566**, 513–517 (2019).
6. Campagne-Ibarcq, P. et al. Quantum error correction of a qubit encoded in grid states of an oscillator. *Nature* **584**, 368–372 (2020).
7. Walschaers, M. Non-Gaussian quantum states and where to find them. *PRX Quantum* **2**, 030204 (2021).
8. Ourjoumtsev, A., Jeong, H., Tualle-Brouri, R. & Grangier, P. Generation of optical ‘Schrödinger cats’ from photon number states. *Nature* **448**, 784–786 (2007).
9. Grimm, A. et al. Stabilization and operation of a Kerr-cat qubit. *Nature* **584**, 205–209 (2020).
10. Lescanne, R. et al. Exponential suppression of bit-flips in a qubit encoded in an oscillator. *Nat. Phys.* **16**, 509–513 (2020).
11. Kenfack, A. & Życzkowski, K. Negativity of the Wigner function as an indicator of non-classicality. *J. Opt. B: Quantum Semiclass. Opt.* **6**, 396 (2004).
12. Wang, Y., Hu, Z., Sanders, B. C. & Kais, S. Qudits and high-dimensional quantum computing. *Front. Phys.* **8**, 589504 (2020).
13. Anderson, B., Sosa-Martinez, H., Riofrío, C., Deutsch, I. H. & Jessen, P. S. Accurate and robust unitary transformations of a high-dimensional quantum system. *Phys. Rev. Lett.* **114**, 240401 (2015).
14. Blok, M. S. et al. Quantum information scrambling on a superconducting qutrit processor. *Phys. Rev. X* **11**, 021010 (2021).
15. Chalopin, T. et al. Quantum-enhanced sensing using non-classical spin states of a highly magnetic atom. *Nat. Commun.* **9**, 4955 (2018).
16. Hrmo, P. et al. Native qudit entanglement in a trapped ion quantum processor. *Nat. Commun.* **14**, 2242 (2023).
17. Gross, J. A. Designing codes around interactions: the case of a spin. *Phys. Rev. Lett.* **127**, 010504 (2021).
18. Gross, J. A., Godfrin, C., Blais, A. & Dupont-Ferrier, E. Hardware-efficient error-correcting codes for large nuclear spins. *Phys. Rev. Appl.* **22**, 014006 (2024).
19. Omanakuttan, S., Buchemavari, V., Gross, J. A., Deutsch, I. H. & Marvian, M. Fault-tolerant quantum computation using large spin-cat codes. *PRX Quantum* **5**, 020355 (2024).
20. Asaad, S. et al. Coherent electrical control of a single high-spin nucleus in silicon. *Nature* **579**, 205–209 (2020).
21. Fernández de Fuentes, I. et al. Navigating the 16-dimensional Hilbert space of a high-spin donor qudit with electric and magnetic fields. *Nat. Commun.* **15**, 1380 (2024).
22. Reck, M., Zeilinger, A., Bernstein, H. J. & Bertani, P. Experimental realization of any discrete unitary operator. *Phys. Rev. Lett.* **73**, 58–61 (1994).
23. Bullock, S. S., O’Leary, D. P. & Brennen, G. K. Asymptotically optimal quantum circuits for d-level systems. *Phys. Rev. Lett.* **94**, 230502 (2005).
24. Leuenberger, M. N. & Loss, D. Grover algorithm for large nuclear spins in semiconductors. *Phys. Rev. B* **68**, 165317 (2003).
25. Faist, P. et al. Continuous symmetries and approximate quantum error correction. *Phys. Rev. X* **10**, 041018 (2020).
26. Cybenko, G. Reducing quantum computations to elementary unitary operations. *Comput. Sci. Eng.* **3**, 27–32 (2001).
27. Gupta, P., Vaartjes, A., Yu, X., Morello, A. & Sanders, B. C. Robust macroscopic Schrödinger’s cat on a nucleus. *Phys. Rev. Res.* **6**, 013101 (2024).
28. Heeres, R. W. et al. Cavity state manipulation using photon-number selective phase gates. *Phys. Rev. Lett.* **115**, 137002 (2015).
29. McKay, D. C., Wood, C. J., Sheldon, S., Chow, J. M. & Gambetta, J. M. Efficient z gates for quantum computing. *Phys. Rev. A* **96**, 022330 (2017).
30. Saeedi, K. et al. Room-temperature quantum bit storage exceeding 39 minutes using ionized donors in silicon-28. *Science* **342**, 830–833 (2013).
31. Muhonen, J. T. et al. Storing quantum information for 30 seconds in a nanoelectronic device. *Nat. Nanotechnol.* **9**, 986–991 (2014).
32. Fröhlichs, F., Sekatski, P., Dür, W., Gisin, N. & Sangouard, N. Macroscopic quantum states: measures, fragility, and implementations. *Rev. Mod. Phys.* **90**, 025004 (2018).
33. Kubischa, E. & Teixeira, I. Permutation-invariant quantum codes with transversal generalized phase gates. Preprint at <https://arxiv.org/abs/2310.17652> (2023).
34. Knill, E. & Laflamme, R. Theory of quantum error-correcting codes. *Phys. Rev. A* **55**, 900 (1997).
35. Lim, S., Liu, J. & Ardavan, A. Fault-tolerant qubit encoding using a spin-7/2 qudit. *Phys. Rev. A* **108**, 062403 (2023).
36. Madzik, M. T. et al. Precision tomography of a three-qubit donor quantum processor in silicon. *Nature* **601**, 348–353 (2022).
37. Jakob, A. M. et al. Scalable atomic arrays for spin-based quantum computers in silicon. *Adv. Mater.* **36**, 2405006 (2024).
38. Morello, A., Pla, J. J., Bertet, P. & Jamieson, D. N. Donor spins in silicon for quantum technologies. *Adv. Quantum Technol.* **3**, 2000005 (2020).
39. Tosi, G. et al. Silicon quantum processor with robust long-distance qubit couplings. *Nat. Commun.* **8**, 450 (2017).
40. Wang, Z. et al. Jellybean quantum dots in silicon for qubit coupling and on-chip quantum chemistry. *Adv. Mater.* **35**, 2208557 (2023).
41. Zwerver, A. et al. Qubits made by advanced semiconductor manufacturing. *Nat. Electron.* **5**, 184–190 (2022).
42. Champion, E., Wang, Z., Parker, R. & Blok, M. Multi-frequency control and measurement of a spin-7/2 system encoded in a transmon qudit. Preprint at <https://arxiv.org/abs/2405.15857> (2024).
43. Roy, S. et al. Synthetic high angular momentum spin dynamics in a microwave oscillator. Preprint at <https://arxiv.org/abs/2405.15695> (2024).
44. Heiss, S. & Weigert, S. Discrete Moyal-type representations for a spin. *Phys. Rev. A* **63**, 012105 (2000).
45. Millen, N. et al. Generalized phase-space techniques to explore quantum phase transitions in critical quantum spin systems. *Ann. Phys.* **458**, 169459 (2023).

Publisher’s note Springer Nature remains neutral with regard to jurisdictional claims in published maps and institutional affiliations.

Springer Nature or its licensor (e.g. a society or other partner) holds exclusive rights to this article under a publishing agreement with the author(s) or other rightsholder(s); author self-archiving of the accepted manuscript version of this article is solely governed by the terms of such publishing agreement and applicable law.

© The Author(s), under exclusive licence to Springer Nature Limited 2025

Methods

Device fabrication

The quantum processor was fabricated using standard Si metal-oxide–semiconductor processes on a 900-nm-thick epilayer of isotopically enriched ^{28}Si (730 ppm residual ^{29}Si) deposited on a natural Si handle wafer. N-type ohmic leads and p-type channels to prevent leakage currents were formed by thermal diffusion of phosphorus and boron, respectively. A central 8-nm-thick high-quality ultra-dry gate oxide and a surrounding 200-nm-thick wet field oxide were grown in oxidation furnaces. $^{123}\text{Sb}^+$ ions (18 keV, $5 \times 10^{11} \text{ cm}^{-2}$) were implanted at normal incidence through a 90 nm \times 100 nm implant window in a poly(methyl methacrylate) mask. A rapid thermal anneal at 1,000 °C for 10 s in a nitrogen atmosphere was performed to repair the implantation damage and activate the donors. Surface nanoelectronics were fabricated as standard for our qubit devices using three layers deposited by electron beam lithography and the deposition of aluminium. Each layer was electrically insulated from the others with native Al_2O_3 , which forms when aluminium is exposed to air. Finally, the sample was annealed in forming gas (400 °C, 15 min, 95% N_2 :5% H_2) to passivate interface traps.

Experimental set-up

The device was wire-bonded to a gold-plated printed circuit board and placed in a copper enclosure. The enclosure was placed in a superconducting solenoid that produced a magnetic field $B_0 = 1.384 \text{ T}$ (see Fig. 1a for the field orientation). The board was mounted on a Bluefors BF-LD400 cryogen-free dilution refrigerator and reached a base temperature of 18 mK.

First, d.c. bias voltages were applied to all gates using voltage sources (SIM928, Stanford Research Systems). A room-temperature resistive combiner was used for the fast donor gates to add d.c. voltages to a.c. signals produced by two analogue output channels of a quantum control and read-out system (OPX+, Quantum Machines), which were then passed through an 80 MHz low-pass filter; all other gates passed through a 20 Hz low-pass filter. All filtering was done at the mixing chamber plate. The wiring included graphite-coated flexible coaxial cables to reduce triboelectric noise⁴⁶.

Microwave pulses to induce electron spin resonance transitions were applied to an on-chip broadband antenna⁴⁷ using a microwave signal generator (E8267D PSG, Keysight). The microwave carrier frequency remained fixed at 38.9426900 GHz, whereas the output frequency was varied within a pulse sequence by mixing it with a radio-frequency (RF) signal using single-sideband modulation, that is by applying RF pulses to the wideband in-phase and quadrature ports of the microwave signal generator's IQ mixer. The digital output channel of the quantum control and read-out system was used to trigger the microwave signal generator. When not triggered, the carrier frequency was expected to be suppressed by 130 dB, according to the data sheet for the signal source. The RF pulses used for single-sideband modulation were generated by two analogue output channels of the quantum control and read-out system. Another analogue output channel of the quantum control and read-out system was used to define the GRF and deliver multi-frequency, phase-coherent, RF pulses to the microwave antenna to drive NMR transitions and apply the multilevel control Hamiltonian. The microwave signal for electron spin resonance and RF signal for NMR were combined in a diplexer (DPX-1721, Marki Microwave).

The set current passed through a transimpedance amplifier (10^7 V A^{-1} gain, 50 kHz bandwidth; DLPCA-200, Femto), followed by a post-amplifier (10^2 V V^{-1} gain; SIM910 JFET, Stanford Research Systems), analogue filter (50 kHz cutoff low-pass Bessel filter; SIM965, Stanford Research Systems), acquired through an analogue input port of the quantum control and read-out system, and then digitized. The measurement instruments were controlled by Python code using the quantum measurement software packages QCoDeS, SiLQ and QUA.

Measurement of dephasing in cat states

To measure the dephasing of z-cat states in different subspaces, we used a generalized Ramsey method⁴⁸. After preparing the cat state $(|m\rangle + | -m\rangle)/\sqrt{2}$ through Givens rotations, we let it evolve freely for a time τ during which it acquired a phase $\xi_{2m}(\tau)$. We then undid the Givens rotations up to the $\pi/2$ pulse, which left the state in a superposition of $(| -m\rangle + e^{i\xi_{2m}(\tau)} | -m+1\rangle)/\sqrt{2}$. A final $\pi/2$ pulse with varying phase depending on τ induced oscillations of the population in the state $| -m\rangle$ that decayed with time. The lifetime T_2^* of the cat state was defined as the time when the initial contrast of this oscillations had decayed to its 1/e point.

Measuring the lifetime of x-oriented cat states is like measuring the lifetime of a spin coherent state. First, applying a covariant $\pi/2$ rotation in the subspace created the spin coherent state along x. By applying a virtual-SNAP gate, the state was transformed into an x-oriented cat state. After free evolution for time τ , we undid the virtual-SNAP gate to revert the state back to a spin coherent state. A final $\pi/2$ pulse with a τ -dependent phase then induced oscillations in $|I_x\rangle(t)$ from which the dephasing time T_2^* was extracted.

When performing operations within subspaces, there is a possibility that the system will leak out of the subspace. This can be caused by imperfect state preparation, by the read-out or by pulse imperfections. As such leakage is easily detected by our read-out process, we discarded experiments in which leakage had occurred.

Data availability

Source data are available via Dryad at <https://doi.org/10.5061/dryad.931zcrjtf> (ref. 49).

Code availability

Scripts to analyse the source data are available via Dryad at <https://doi.org/10.5061/dryad.931zcrjtf> (ref. 49).

References

46. Kalra, R. et al. Vibration-induced electrical noise in a cryogen-free dilution refrigerator: characterization, mitigation, and impact on qubit coherence. *Rev. Sci. Instrum.* **87**, 073905 (2016).
47. Dehollain, J. et al. Nanoscale broadband transmission lines for spin qubit control. *Nanotechnology* **24**, 015202 (2012).
48. Godfrin, C. et al. Generalized Ramsey interferometry explored with a single nuclear spin qudit. *npj Quantum Inf.* **4**, 53 (2018).
49. Yu, X. et al. Schrödinger cat states of a nuclear spin qudit in silicon. Dryad <https://doi.org/10.5061/dryad.931zcrjtf> (2024).

Acknowledgements

We thank J. A. Gross, V. Scarani, J. Marshall and J. Saied for insightful discussions. The research was funded by an Australian Research Council Discovery Project (Grant No. DP210103769), the US Army Research Office (Contract No. W911NF-23-1-0113) and the Australian Department of Industry, Innovation and Science (Grant No. AUSMURIO000002). We acknowledge the facilities and the scientific and technical assistance provided by the UNSW node of the Australian National Fabrication Facility (ANFF) and by the Heavy Ion Accelerators (HIA) nodes at the University of Melbourne and the Australian National University. ANFF and HIA are supported by the Australian Government through the National Collaborative Research Infrastructure Strategy programme. Ion beam facilities employed by D.N.J. and A.M.J. were co-funded by the Australian Research Council Centre of Excellence for Quantum Computation and Communication Technology (Grant No. CE170100012). X.Y., B.W., M.R.V.B. and A.V. acknowledge support from the Sydney Quantum Academy. D.N.J. acknowledges the support of a Royal Society (UK) Wolfson Visiting Fellowship (RSWVF/211016). P.G. and B.C.S. acknowledge funding from the Natural Sciences and Engineering Research Council of Canada, Alberta Innovates and the Government of Alberta. N.A. is a KBR

employee working under Prime Contract No. 80ARCO20D0010 with the NASA Ames Research Center and is grateful for the collaborative agreement between NASA and CQC2T. The views and conclusions contained in this document are those of the authors and should not be interpreted as representing the official policies, either expressed or implied, of the Army Research Office or the US Government. The US Government is authorized to reproduce and distribute reprints for government purposes notwithstanding any copyright notation herein. Sandia National Laboratories is a multimission laboratory managed and operated by National Technology & Engineering Solutions of Sandia, LLC, a wholly owned subsidiary of Honeywell International Inc., for the US Department of Energy's National Nuclear Security Administration under contract DE-NA0003525. This paper describes objective technical results and analysis. Any subjective views or opinions that might be expressed in the paper do not necessarily represent the views of the US Department of Energy or the United States Government.

Author contributions

X.Y., B.W., A.V., D.S., M.N., D.H., A.K., M.R.v.B. and A.M. conceived and designed the experiments, with theoretical input from P.G., B.C.S. and N.A. X.Y., B.W., A.V., M.N., D.H., D.S., A.K. and M.R.v.B. performed and analysed the measurements. D.H. and F.E.H. fabricated the device under A.S.D.'s supervision using materials supplied by K.M.I. A.M.J., D.H. and D.N.J. designed and performed the ion implantation. R.J.M., R.B.-K. and T.D.L. contributed to the data analysis. A.M., X.Y., B.W., D.H.,

A.V., R.B.-K., P.G., T.D.L. and N.A. wrote the manuscript with input from all co-authors. A.M. supervised the project.

Competing interests

A.M. is an inventor on a patent related to this work. The patent describes the use of high-spin donor nuclei as quantum information processing elements (Application Nos. AU2019227083A1, US16/975,669 and WO2019165494A1). A.S.D. is the chief executive officer and a director of Diraq Pty Ltd. F.E.H. and A.S.D. declare an equity interest in Diraq Pty Ltd. The other authors declare no competing interests.

Additional information

Supplementary information The online version contains supplementary material available at <https://doi.org/10.1038/s41567-024-02745-0>.

Correspondence and requests for materials should be addressed to Andrea Morello.

Peer review information *Nature Physics* thanks John Morton and the other, anonymous, reviewer(s) for their contribution to the peer review of this work.

Reprints and permissions information is available at www.nature.com/reprints.

Schrödinger cat states of a nuclear spin qudit in silicon

In the format provided by the
authors and unedited

CONTENTS

SI: 1. Introduction to spin coherent states	2
SI: 2. Spin Wigner function	3
A. Definition and Wigner negativity	3
B. Quantifying Wigner negativity	3
C. Spin coherent states vs Schrödinger cat states	4
D. Visualizing quantum states with Wigner functions	5
E. Phase shifts and fringe patterns in the Wigner function	8
SI: 3. Schrödinger cat code	10
A. Spin-cat code	10
B. Error correction	11
C. Logical gates	11
SI: 4. Covariant $SU(2)$ rotation theory	12
A. Generalised rotating frame	12
B. Multi-frequency driving pulse	12
C. Power dependence of covariant $SU(2)$ rotations	14
SI: 5. SNAP gates and qudit universality	15
SI: 6. Creation of spin cat states with virtual-SNAP gate	16
A. Arbitrary virtual-SNAP gates on the nuclear spin	16
B. Implementation of one-axis twisting by virtual-SNAP	17
SI: 7. Subspace rotations and different size cat states	18
SI: 8. Parity measurement	20
SI: 9. Density matrix reconstruction	21
A. Tomographic measurement protocol	21
B. Maximum likelihood state estimation	21
C. Confirming the validity of the state tomography	23
SI: 10. T_2^* for adjacent nuclear spin levels	25
SI: 11. Nuclear spin readout and initialisation	25
A. Electron initialisation via a Maxwell's demon	26
B. Nuclear quantum jumps - deviation from QND nuclear readout	26
SI: 12. Other devices	28
References	29

SI: 1. INTRODUCTION TO SPIN COHERENT STATES

There are several excellent references that discuss the notion of spin coherent states and quasiprobability distributions (e.g., the classic reference [1]). The discussion below follows mixed conventions, borrowing from Refs. [2, 3]. We pedagogically revisit these for completeness, see also a recent work [4] that discusses various notions of quantumness, for both optical and spin systems.

We will focus on a $(2I + 1)$ -dimensional Hilbert space, \mathcal{H}_I which can host an irreducible representation of the Lie algebra $\mathfrak{su}(2)$ [5]. Physically, these systems can be thought of as a *qudit* with dimension, $d = 2I + 1$ (although the equal spacing of energy levels can make their control *nontrivial*). The Lie algebra $\mathfrak{su}(2)$ is generated by the operators, $\{\hat{I}_x, \hat{I}_y, \hat{I}_z\}$ satisfying the canonical “spin” commutation relations,

$$[\hat{I}_x, \hat{I}_y] = i\epsilon_{xyz}\hat{I}_z, \quad (1)$$

where ϵ_{xyz} is the Levi-Cevita tensor, capturing the cyclicity of the commutation relations. The Casimir operator (total spin) is

$$\hat{I}^2 = \hat{I}_x^2 + \hat{I}_y^2 + \hat{I}_z^2 = I(I+1)\mathbb{I}$$

and commutes with all elements of the Lie algebra and is a natural choice for labeling various quantum states via “good quantum numbers”. Recall that I can be (half-)integer. The Hilbert space \mathcal{H}_I is spanned by the (simultaneous) eigenbasis of \hat{I}^2 and \hat{I}_z , namely,

$$\mathcal{H}_I = \text{span}\{|I, m_I\rangle \mid m_I = -I, -I+1, \dots, I-1, I\}, \quad (2)$$

with m_I going in integer steps. These states are often called “Dicke states” and are uniquely identified via relations,

$$\begin{aligned} \hat{I}^2|I, m_I\rangle &= I(I+1)|I, m_I\rangle \\ \hat{I}_z|I, m_I\rangle &= m_I|I, m_I\rangle. \end{aligned}$$

The raising and lowering operators defined as $\hat{I}_{\pm} := \hat{I}_x \pm i\hat{I}_y$ act on the basis states as,

$$\begin{aligned} \hat{I}_+|I, m_I\rangle &= \sqrt{(I-m_I)(I+m_I+1)}|I, m_I+1\rangle \\ \hat{I}_-|I, m_I\rangle &= \sqrt{(I+m_I)(I-m_I+1)}|I, m_I-1\rangle. \end{aligned}$$

The lowest and highest weight states are $|I, -I\rangle$, $|I, I\rangle$, respectively, and form natural candidates for studying the “phase space” associated to the Lie group $SU(2)$. When defining spin coherent states, one chooses as the reference, either the lowest or the highest weight state. In this work, we choose the highest weight state as the reference $|I, I\rangle$.

The natural phase space to describe these family of transformations is $SU(2)/U(1) \cong S^2$, i.e., the Bloch sphere. Let us define the “spin displacement operator” in analogy to the displacement unitary in quantum optics as (also known as the covariant $SU(2)$ rotation in the rest of this text),

$$\hat{D}(\theta, \varphi) = \exp\left[\frac{\theta}{2}\left(e^{i\varphi}\hat{I}_- - e^{-i\varphi}\hat{I}_+\right)\right]. \quad (3)$$

If we define the $\vec{n} = (\sin\theta\cos\varphi, \sin\theta\sin\varphi, \cos\theta)$ then, $SU(2)$ coherent states (hereafter “spin coherent states” (SCS)) are defined as “global rotations” of the reference state, namely,

$$|\vec{n}\rangle = \hat{D}(\vec{n})|I, I\rangle, \quad (4)$$

where θ, φ represent the spherical coordinates of the unit vector \vec{n} on the Bloch sphere. It is worthwhile to note two important properties of SCS:

1. Non-orthogonality (just like optical coherent states):

$$\left|\langle \vec{n}_1 | \vec{n}_2 \rangle\right|^2 = \left[\frac{1}{2}(1 + \vec{n}_1 \cdot \vec{n}_2)\right]^{2I}. \quad (5)$$

Although, unlike optical coherent states, for any $(2I + 1)$ -dimensional representation, we always have at least two SCS that are orthogonal, the lowest and the highest weight representations, $|I, -I\rangle$, $|I, I\rangle$, respectively. This, as we will see shortly, implies that $SU(2)$ Wigner functions must have some amount of negativity even for SCS, in contrast with the famous Hudson’s theorem for optical coherent states [6], which tells us that optical coherent states have zero Wigner negativity.

2. Overcompleteness (also, like optical coherent states):

$$\frac{2I+1}{4\pi} \int_{S^2} d\vec{n} |\vec{n}\rangle \langle \vec{n}| = \mathbb{I}. \quad (6)$$

As a final remark, we note that the algebra of spins can be thought of as a “hard cutoff” on the Heisenberg-Weyl algebra underlying optical coherent states [7].

SI: 2. SPIN WIGNER FUNCTION

A. Definition and Wigner negativity

The Wigner function is a widely used tool for representing the joint quasi-probability distribution of position and momentum variables, denoted as $\{\hat{x}, \hat{p}\}$, on a planar phase space. Because \hat{x} and \hat{p} do not commute in quantum mechanics, the value of the Wigner function can be negative. Negativity is commonly regarded as a signature of nonclassicality. The natural phase space of the Wigner function for the $SU(2)$ group is a sphere S^2 as discussed above. To define the Wigner function, following Refs. [8, 9] we use the $SU(2)$ kernel operator at some phase space point (θ, φ) as,

$$\Delta(\theta, \varphi) := \sum_{m_I=-I}^I \Delta_{I,m_I} \hat{\mathcal{D}}(\theta, \varphi) |I, m_I\rangle \langle I, m_I| \hat{\mathcal{D}}^\dagger(\theta, \varphi), \quad (7)$$

where $\hat{\mathcal{D}}(\theta, \varphi)$ is the covariant $SU(2)$ rotation and

$$\Delta_{I,m_I} = \sum_{\ell=0}^{2I} \frac{2\ell+1}{2I+1} \left\langle \begin{array}{cc} j & \ell \\ m_I & 0 \end{array} \middle| \begin{array}{c} I \\ m_I \end{array} \right\rangle \quad (8)$$

with $\left\langle \begin{array}{cc} j & \ell \\ m_I & 0 \end{array} \middle| \begin{array}{c} I \\ m_I \end{array} \right\rangle$ the usual Clebsch-Gordon coefficients. With the $SU(2)$ kernel, the Wigner function of a quantum state ρ at the phase space point θ, φ is simply the expectation value of this operator, namely,

$$W_\rho(\theta, \varphi) := \text{tr}[\rho \Delta(\theta, \varphi)]. \quad (9)$$

Equivalently, we can express the Wigner function in terms of the spherical harmonics $Y_{\ell,m}(\theta, \varphi)$ as discussed in the visualization section SI: 2D.

This entire section uses $|I, m_I\rangle$ for the Dicke states as opposed to $|j\rangle, |S\rangle$ to be consistent with the previous notation. Majority of these results were obtained in Refs. [8, 9]. First we note that Wigner functions for SCS must have Wigner negativity in all dimensions. This follows from the fact that, for any $d = 2I + 1$, we have two quantum states, $|I, I\rangle$ and $|I, -I\rangle$ such that $|\langle I, I|I, -I\rangle|^2 = 0$. Translating this into the inner product of their Wigner functions, we have,

$$0 = |\langle I, I|I, -I\rangle|^2 = \int_{S^2} W_{|I,I\rangle}(\theta, \varphi) W_{|I,-I\rangle}(\theta, \varphi) d\Omega, \quad (10)$$

where $d\Omega = \frac{2I+1}{4\pi} \sin(\theta) d\theta d\varphi$. Notice that since $|I, \pm I\rangle$ are normalized quantum states, their Wigner functions cannot be identically zero. This combined with the fact that the integral above has to vanish, implies that one of the Wigner functions must be negative (in some regions). Namely, the above equality cannot be satisfied by two strictly positive functions, and therefore they must become negative somewhere [10]. This observation holds for all dimensions and therefore the $SU(2)$ Wigner function is negative in all finite d . Notice that the same argument *does not* apply to optical Wigner functions (of pure states) since any two optical coherent states are only orthogonal in the $\alpha \rightarrow \infty$ limit and so for any finite region of the phase space, we do not suffer from this issue.

B. Quantifying Wigner negativity

An important detail in the quantification of the Wigner negativity is the choice of normalization for the spin Wigner function. Following Refs. [8, 9], we choose the normalization as follows,

$$\int_{S^2} W_\rho(\theta, \varphi) d\Omega = \frac{(2I+1)}{4\pi} \int_{\theta=0}^{\pi} \int_{\varphi=0}^{2\pi} W_\rho(\theta, \varphi) \sin(\theta) d\theta d\varphi = 1. \quad (11)$$

Namely, we choose $d\Omega = \frac{(2I+1)}{4\pi} \sin(\theta) d\theta d\varphi$ as the uniform measure. This ensures that the Wigner function for any spin- I irrep and any quantum state is always normalized to one. One could of course divide the Wigner function to ensure that we just need to integrate over the uniform measure on the sphere (and no other prefactor), but we stick with the above normalization to be consistent with the results of Refs. [8, 9].

To compute the total negative regions of the $SU(2)$ Wigner function (a.k.a. the Wigner negativity “volume”), we define the Wigner negativity as [9],

$$\mathcal{N}_\psi = \frac{1}{2} \int_{S^2} \left(|W_\psi(\theta, \varphi)| - W_\psi(\theta, \varphi) \right) d\Omega = \frac{1}{2} \left(\int_{S^2} |W_\psi(\theta, \varphi)| d\Omega - 1 \right). \quad (12)$$

We again emphasize that the measure used above is $d\Omega = \frac{(2I+1)}{4\pi} \sin(\theta) d\theta d\varphi$, with an additional factor of $(2I+1)/(4\pi)$ along with the uniform measure on the sphere. This is analogous to the negativity in quantum entanglement, obtained via a partial transpose as,

$$\mathcal{N}(\rho) \equiv \frac{\|\rho^{\Gamma_A}\|_1 - 1}{2}, \quad (13)$$

where ρ^{Γ_A} is the partial transpose of ρ w.r.t. subsystem A. Writing in terms of the eigenvalues makes the connection more transparent as $\mathcal{N}(\rho) = \frac{1}{2} \sum_j (|\lambda_j| - \lambda_j)$ where λ_j are the eigenvalues of ρ^{Γ_A} , which can now be negative. We can also define the logarithmic Wigner negativity (just as in entanglement theory) as,

$$\mathcal{L}_\psi := \log_2(2\mathcal{N}_\psi + 1). \quad (14)$$

This is essentially the quantity that is plotted in the Fig. S1 since we are on a log-linear scale. We numerically find the universal decay for the Wigner negativity as $\mathcal{N} \propto \frac{1}{I^2}$ (notice this is not for the log-Wigner negativity which would be a linear function).

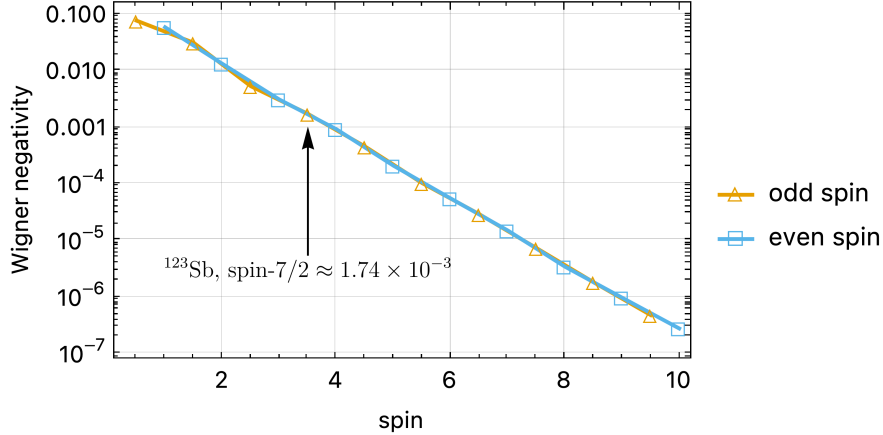


FIG. S1. **Wigner negativity for spin qudits $I \in [1/2, 1, 3/2, \dots, 10]$ plotted on a log-linear scale.** The even and odd curves decay as a power-law and converge to a universal decay rate of $\mathcal{N} \propto I^{-2}$. This implies that the volume of Wigner negative regions goes to zero only as $I \rightarrow \infty$.

C. Spin coherent states vs Schrödinger cat states

For the SCS, a closed form expression for the Wigner function was obtained in [8, 9]. Since all SCS are connected via global rotations, we choose to focus on the SCS at the north pole [9],

$$W_{|I,I\rangle}(\theta, \varphi) = \frac{(2I)!}{\sqrt{2I+1}} \sum_{\ell=0}^{2I} \frac{(2\ell+1)}{\sqrt{(2I-\ell)!(2I+1+\ell)!}} P_\ell(\cos \theta), \quad (15)$$

where $P_\ell(\cdot)$ is the Legendre polynomial of degree ℓ . Notice that the Wigner function is only a function of the θ . We numerically compute the Wigner negativity for SCS in Fig. S1. By numerically fitting the curve, we find a universal

decay rate of the Wigner negativity as $\mathcal{N} \propto I^{-2}$, which implies that volume of Wigner negative regions goes to zero as $I \gg 1$. This is consistent with what one would expect from Hudson's theorem for optical coherent states (namely that they should have zero Wigner negativity for pure coherent states).

To compute the Wigner negativity of cat states, we again utilize the results of Ref. [9]. They consider cat states of the form $|\text{cat}_I\rangle_{\vartheta,\xi_{2I}} := \cos\left(\frac{\vartheta}{2}\right)|I, I\rangle + e^{i\xi_{2I}} \sin\left(\frac{\vartheta}{2}\right)|I, -I\rangle$. We are interested in the case of $\vartheta = \pi/2, \xi_{2I} = 0$ which gives us the cat state $|\text{cat}_I\rangle_z := \frac{1}{\sqrt{2}}(|I, I\rangle + |I, -I\rangle)$. The Wigner negativity of this state is obtained as an analytical expression as,

$$W_{|\text{cat}_I\rangle_z}(\theta, \varphi) = \frac{1}{2} \left(W_{|I, I\rangle}(\theta, \varphi) + W_{|I, -I\rangle}(\theta, \varphi) \right) + \frac{1}{2^{2I}(2I)!} \underbrace{\sqrt{\frac{(4I+1)!}{2I+1}} (\sin(\theta))^{2I} \cos(2I\varphi)}_{\text{interference term}}. \quad (16)$$

Most of the Wigner negativity for this state comes from the “interference term,” as the Wigner negativity of the SCS vanishes in large- I limit. We also briefly use the fact that the Wigner negativity of a Dicke state has the form [8],

$$W_{|I, m_I\rangle}(\theta, \varphi) = \sum_{l=0}^{2I} \frac{2l+1}{2I+1} \left\langle \begin{array}{cc} I & l \\ m_I & 0 \end{array} \middle| \begin{array}{c} I \\ m_I \end{array} \right\rangle P_l(\cos \theta), \quad (17)$$

In Ref. [9] the authors also utilized bounds on the Wigner negativity of (half-)integer cat states as,

$$\mathcal{N}^{(\text{int})} \lesssim \frac{1}{\pi} \sqrt{\frac{(4I+1)!}{2I+1}} \left(\frac{I!}{(2I)!} \right)^2 \quad (18)$$

$$\mathcal{N}^{(\text{half-int})} \lesssim \sqrt{\frac{(4I+1)!}{2I+1}} \frac{1}{2^{4I}} \frac{1}{(I-\frac{1}{2})!^2}. \quad (19)$$

We plot these bounds along with the actual values of Wigner negativity obtained via numerical integration in Fig. S2. We find (as noticed in [9]) that around $I \gtrsim 7$ the bound is essentially exact.

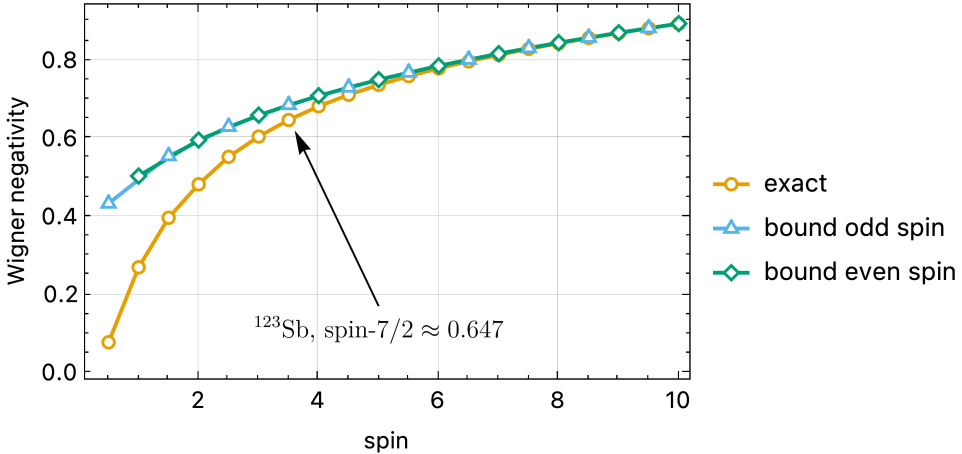


FIG. S2. **Wigner negativity for cat states of spin qudits** $I \in [1/2, 1, 3/2, \dots, 10]$. The even and odd curves are obtained via a bound and converge to the numerical integration value around $I \gtrsim 7$. From numerical simulations, it appears that the Wigner negativity is monotonically increasing with I and does not converge to a fixed value in the large- I limit (although, one can potentially redefine operators that allows to converge to the optical cat state Wigner negativity in the large- I limit).

A final note about the Wigner negativity of cat states vs. coherent states: From numerical simulations, even at spin- $I = 10$, the Wigner negativity of a coherent state is $\approx 10^{-7}$ while that for a cat state is ≈ 1 . As $I \gg 1$, the Wigner negativity for SCS essentially vanishes while that for cat states slowly grows larger and larger but remains around $O(1)$.

D. Visualizing quantum states with Wigner functions

The Wigner function serves as a convenient tool for visualising states in high-dimensional systems, particularly for highlighting highly non-classical states that exhibit distinct fringe patterns and negativity. In this section and in the

main text, we use the following normalization for the Wigner function:

$$W_\rho(\theta, \varphi) = \sqrt{\frac{2}{\pi}} \sum_{k=0}^{2I} \sum_{q=-k}^k Y_{kq}(\theta, \varphi) \rho_{kq}, \quad (20)$$

where Y_{kq} are the spherical harmonics and ρ_{kq} is an element of the density matrix decomposed in the spherical harmonic basis [11]. This equation shows that W is entirely determined by the density matrix ρ and can therefore be reconstructed using quantum state tomography (see SI: 9). Note that the normalization here is different from that in the previous sections. We use QuTiP for numerical simulations and they use a slightly different normalization [12, 13], which is simply an overall factor of $\pi\sqrt{2}/\sqrt{d}$.

Despite the finite-dimensional nature of high-spin states, they bear a strong resemblance to quantum optical states in 2D continuous phase space. In Fig. S3 we provide examples of 3D spherical Wigner functions of high-spin states, complemented by their corresponding planar representations utilising Hammer and polar projections. In addition, we provide 2D Wigner functions representing bosonic states in quantum optics to provide a side-by-side comparison and highlight a few compelling analogies with high-spin states.

In particular, there is a clear resemblance between spin coherent states and bosonic coherent states, or between spin projection eigenstates $|m_I\rangle$ and bosonic Fock states $|N\rangle$. This analogy is particularly evident in the polar projection for spin states. For Schrödinger cat states, spin and bosonic states exhibit similar interference patterns, which can be oriented along different directions – x and z for spins, x (or $\text{Re}(\alpha)$) and p (or $\text{Im}(\alpha)$) for bosons. Here, the analogy is most evident when comparing the spin Hammer projection to the phase-space representation of bosonic modes.

However, the analogy is not all-encompassing. For example, the action of a bosonic displacement operator, $\hat{\mathcal{D}}$, is closely analogous to the effect of a covariant $SU(2)$ rotation (CR) on a spin coherent state, but this optical analogy does not hold when considering the fact that a covariant $\pi/2$ spin rotation can turn $|\text{cat}_I\rangle_x$ to $|\text{cat}_I\rangle_y$. In the bosonic case, the rotation would require a phase shift instead of a displacement.

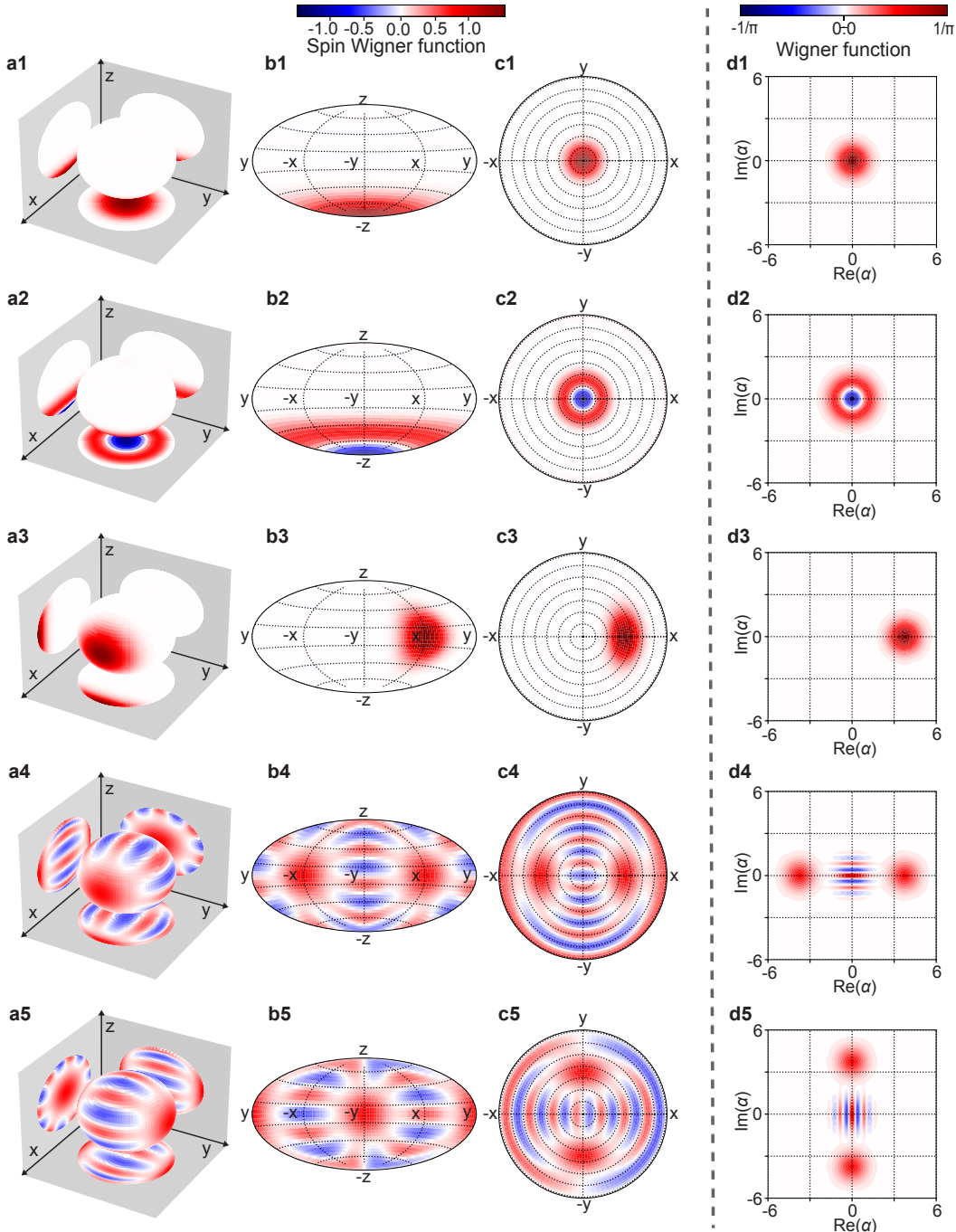


FIG. S3. Comparison of Wigner functions in high-spin states and bosonic states in quantum optics. **a**, 3D spherical spin Wigner functions in an 8-dimensional Hilbert space. The grey planes in the Wigner plots show the mirrored reflections of the sphere. The projection plots **b**, 2D Hammer projections of the spherical Wigner functions. **c**, 2D Polar projections of the spherical Wigner functions, observed from the south pole (the north pole becomes the outer circle). **d**, Wigner functions for a bosonic mode, where α is an arbitrary complex number, describing the displacement from the vacuum state. The following states are represented: **a1-c1**, $| -7/2 \rangle$; **d1**, vacuum state $| 0 \rangle$, **a2-c2**, $| -5/2 \rangle$, containing one spin excitation from the $| -7/2 \rangle$ state; **d2**, Fock state $| 1 \rangle$, i.e. a bosonic mode containing one photon; **a3-c3**, $| scs_{7/2} \rangle_x$, a spin coherent state pointing maximally along x ; **d3**, displaced coherent state $(\hat{D}(\sqrt{7})| 0 \rangle)$. In rows 1,2 and 3, note the similarity between spin and bosonic states, especially evident in the polar projections. **a4-c4**, x -oriented Schrödinger cat state $| cat_{7/2} \rangle_x = (| 7/2 \rangle_x + | -7/2 \rangle_x) / \sqrt{2}$; **d4**, x -oriented bosonic cat state $\frac{1}{\sqrt{2}}(\hat{D}(\sqrt{7}i)| 0 \rangle + \hat{D}(-\sqrt{7}i)| 0 \rangle)$; **a5-c5**, y -oriented Schrödinger cat state $| cat_{7/2} \rangle_y = (| 7/2 \rangle_y + | -7/2 \rangle_y) / \sqrt{2}$, **d5**, p -oriented bosonic cat state $\frac{1}{\sqrt{2}}(\hat{D}(\sqrt{7})| 0 \rangle + \hat{D}(-\sqrt{7})| 0 \rangle)$.

E. Phase shifts and fringe patterns in the Wigner function

The fringe pattern in the Wigner function captures the phase information contained in a quantum state. Consider the two-component spin cat states $|\text{cat}_{7/2}\rangle_n$, which take the form

$$|\text{cat}_{7/2}\rangle_n = \frac{1}{\sqrt{2}} \left(|\text{scs}_{7/2}\rangle_n + e^{i\xi_7} |\text{scs}_{7/2}\rangle_{-n} \right), \quad (21)$$

where $|\text{scs}_{7/2}\rangle_n$ and $|\text{scs}_{7/2}\rangle_{-n}$ are two anti-parallel spin coherent states, oriented along the unit vectors \mathbf{n} and $-\mathbf{n}$ in the spin-7/2 Bloch sphere. The dependence on the phase factor $e^{i\xi_7}$ indicates that a cat state is *not* uniquely defined by the position of its ‘heads’. We further illustrate this point by inspecting the Wigner functions of cat states of along the z and x axes, denoted as $|\text{cat}_{7/2}\rangle_z$ and $|\text{cat}_{7/2}\rangle_x$ respectively.

In Fig. S4 we plot the Wigner functions $W_\rho(\theta, \varphi)$ of three z -cats, distinguished by their different values of $\xi_7 = 0, \pi/2, \pi$. Under each Hammer projection of the Wigner plot, we draw a line-cut around the equator. This figure highlights that all $|\text{cat}_{7/2}\rangle_z$ states always display 7 periods of oscillations around the equator, and the phase ξ_7 determines the phase of such oscillations. Therefore, even though all these states have their ‘heads’ located at $+z$ and $-z$, they can be distinguished by the phase of the oscillations of the Wigner function around the equator.

In Fig. S5 we plot the value of the Wigner function of $|\text{cat}_{7/2}\rangle_z = (|7/2\rangle + e^{i\xi_7} |-7/2\rangle) / \sqrt{2}$ at a fixed location on the Bloch sphere, namely $(\theta = \pi/2, \varphi = -\pi/2)$, (marked as a yellow star in Fig. S4a), as a function of $\xi_7 \in [-\pi, \pi]$. Here we note that a full 2π sweep of the phase ξ_7 results in only one period of oscillation of $W_\rho(\pi/2, -\pi/2)$, despite the presence of 7 oscillations along the equatorial axis φ in Fig. S4a. In other words, it only takes $1/7$ of a rotation of the Wigner function to cover the whole range of phases ξ_7 .

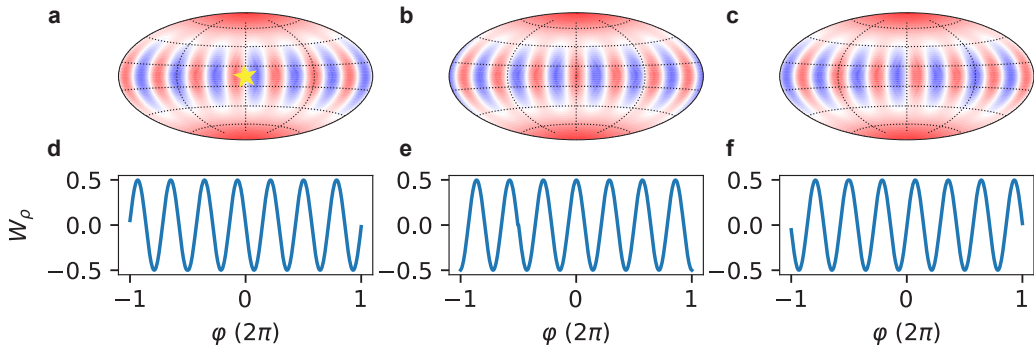


FIG. S4. Phase dependence of the Wigner function of a z -oriented spin-cat state. Hammer projection of the Wigner function of $|\text{cat}_{7/2}\rangle_z = (|7/2\rangle + e^{i\xi_7} |-7/2\rangle) / \sqrt{2}$ for **a** $\xi_7 = 0$, **b** $\xi_7 = \pi/2$, and **c** $\xi_7 = \pi$. **d-f** Equatorial line-cuts of the Wigner functions in **a-c**.

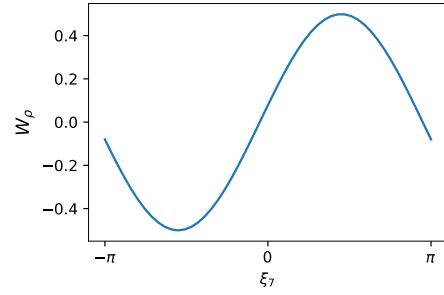


FIG. S5. Wigner function of a z -cat at $(\pi/2, -\pi/2)$ as a function of phase ξ_7 .

Next we consider the cat states along the x direction, $|\text{cat}_{7/2}\rangle_x = (|\text{scs}_{7/2}\rangle_x + e^{i\xi_7} |\text{scs}_{7/2}\rangle_{-x}) / \sqrt{2}$, where $|\text{scs}_{7/2}\rangle_{\pm x}$ represent spin coherent states along the $\pm x$ direction. We illustrate three examples of $|\text{cat}_{7/2}\rangle_x$ states for different phases, $\xi_7 = 0, \pi/2, \pi$. In the notation used in Section SI: 3B, $\xi_7 = 0$ yields the $|\text{cat}_{7/2}^+\rangle_x$ state, and $\xi_7 = \pi$ yields

the $|\text{cat}_{7/2}^-\rangle_x$. As shown in Fig. S6, the ‘heads’ of the cat remain fixed regardless of the phase ξ_7 , whereas the fringe patterns along the polar axis θ vary with ξ_7 . Line-cuts along the meridian at fixed longitude $\varphi = -\pi/2$ display oscillations in the Wigner function whose phase depends on the chosen value of ξ_7 , just like in the z -cat case. Since we plot θ from 0 to π , only 3.5 oscillation periods are seen instead of 7. Again, fixing the point $(\theta = \pi/2, \varphi = -\pi/2)$ (yellow star in Fig. S6a) and sweeping the phase $\xi_7 \in [-\pi, \pi]$ in the state $|\text{cat}_{7/2}\rangle_x$ results in a single-period oscillation for $W_\rho(\pi/2, -\pi/2)$ (Fig. S7).

There is, however, a crucial difference between x -cats and z -cats. Whereas in the z case the phase ξ_7 only determines the phase of the Wigner function oscillations, in the x case it also *changes the populations* of the eigenstates $|m_I\rangle$ (Fig. S8) and, as consequence, the parity of the state. Below we show explicitly the populations of three representative states, for $\xi_7 = 0$, $\xi_7 = \pi/2$, and $\xi_7 = \pi$, resulting in even, zero, and odd parities.

$$|\text{cat}_{7/2}, \xi_7 = 0\rangle_x = \begin{pmatrix} 0.125 \\ 0 \\ 0.573 \\ 0 \\ 0.740 \\ 0 \\ 0.331 \\ 0 \end{pmatrix} \quad (22a)$$

$$|\text{cat}_{7/2}, \xi_7 = \pi/2\rangle_x = \begin{pmatrix} -0.088 \times e^{-i\frac{3\pi}{4}} \\ 0.234 \times e^{-i\frac{\pi}{4}} \\ -0.405 \times e^{-i\frac{3\pi}{4}} \\ 0.523 \times e^{-i\frac{\pi}{4}} \\ -0.523 \times e^{-i\frac{3\pi}{4}} \\ 0.405 \times e^{-i\frac{\pi}{4}} \\ -0.234 \times e^{-i\frac{3\pi}{4}} \\ 0.088 \times e^{-i\frac{\pi}{4}} \end{pmatrix} \quad (22b)$$

$$|\text{cat}_{7/2}, \xi_7 = \pi\rangle_x = \begin{pmatrix} 0 \\ 0.331 \\ 0 \\ 0.740 \\ 0 \\ 0.573 \\ 0 \\ 0.125 \end{pmatrix} \quad (22c)$$

In particular, when $\xi_7 = \pm\pi/2$, the cat states along x direction exhibit the same state population as the spin coherent state along the equator. Within the generalised rotating frame, a virtual-SNAP gate can only create cat states with identical populations as a spin coherent state along the equator, as detailed in Section SI: 6.

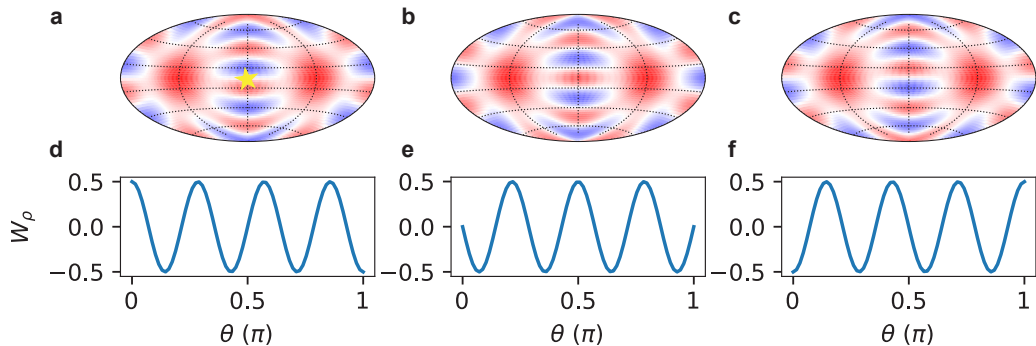


FIG. S6. Phase dependence of the Wigner function of a spin-cat state along x axis. **a-c** show the plots of the Wigner function of $|\text{cat}_{7/2}\rangle_x = (|7/2\rangle_x + e^{i\xi_7} |-7/2\rangle_x)/\sqrt{2}$ for different phases ξ_7 . **a**, $\xi_7 = 0$, **b**, $\xi_7 = \pi/2$, and **c**, $\xi_7 = \pi$. **d-f** show the corresponding polar line-cuts of the Wigner function $W_\rho(\theta, -\pi/2)$ highlighting the oscillation in the Wigner function along the polar line.

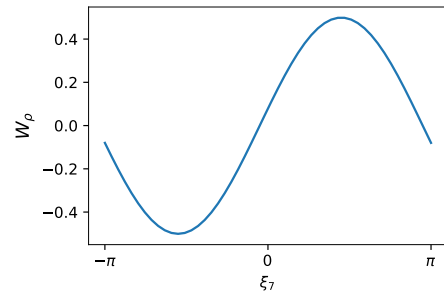


FIG. S7. Wigner function of an x -cat at $(\pi/2, -\pi/2)$ as a function of phase ξ_7 .

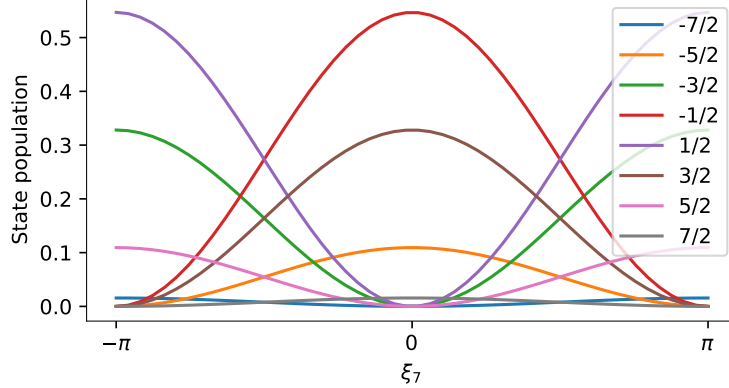


FIG. S8. **Phase-dependent state populations for an x -cat.** The population of the $|m_I\rangle$ states is plotted as a function of the phase ξ_7 for a $|\text{cat}_{7/2}\rangle_x$ state.

SI: 3. SCHRÖDINGER CAT CODE

Hardware-efficient error correcting codes on a high-dimensional quantum object utilise the large Hilbert space of a single system, such as a harmonic oscillator, instead of multiple qubits to protect quantum information from dominant errors. In particular, bosonic codes can be used to correct errors such as photon loss, photon dephasing and thermal excitations by encoding information in the phase space of a harmonic oscillator [14]. One such code is the two-component cat code [15], defined by the Schrödinger cat states

$$|\mathcal{C}_\alpha^\pm\rangle = \frac{|\alpha\rangle \pm |-\alpha\rangle}{\sqrt{2(1 \pm e^{-2|\alpha|^2})}}, \quad (23)$$

where $|\alpha\rangle$ is a coherent state of the bosonic mode, and α is an arbitrary complex number describing the displacement from the vacuum state. The cat state $|\mathcal{C}_\alpha^+\rangle$ only contains even Fock states and $|\mathcal{C}_\alpha^-\rangle$ only contains odd Fock states, and the encoded states are given by

$$|0\rangle = \frac{1}{\sqrt{2}} (|\mathcal{C}_\alpha^+\rangle + |\mathcal{C}_\alpha^-\rangle) = |\alpha\rangle + \mathcal{O}(\exp(-2|\alpha|^2)), \quad (24)$$

$$|1\rangle = \frac{1}{\sqrt{2}} (|\mathcal{C}_\alpha^+\rangle - |\mathcal{C}_\alpha^-\rangle) = |-\alpha\rangle + \mathcal{O}(\exp(-2|\alpha|^2)), \quad (25)$$

where the separation in the phase space between the codewords can be tuned by the amplitude $|\alpha|$ of the component coherent states. The bosonic cat code can suppress bit-flip errors exponentially with $|\alpha|^2$, while increasing the phase-flip error rate only linearly, and can help reduce the hardware overhead for fault tolerant quantum computation. Another approach for designing hardware-efficient codes is to take advantage of the redundancy in the Hilbert space of a qudit, where the multiple levels can be used to encode information within a single finite-dimensional system. Here, we consider an error correction code based on Schrödinger cat states in a single spin- I system, with $2I+1$ levels, for protecting information against dephasing of the spin.

A. Spin-cat code

Schrödinger cat states on a single spin are superpositions of maximally separated quasi-classical states, i.e. spin coherent states (scs), along any axis of the spin. Here we consider an encoding based on cat states along the x -axis

$$|\text{cat}_I^\pm\rangle_x = \frac{1}{\sqrt{2}} (|\text{scs}_I\rangle_{-x} \pm |\text{scs}_I\rangle_x), \quad (26)$$

where $|\bar{0}\rangle := |\text{scs}_I\rangle_{-x} = |I, -I\rangle_x$ and $|\bar{1}\rangle := |\text{scs}_I\rangle_x = |I, I\rangle_x$ are spin coherent states oriented along the $-x$ and $+x$ axes, respectively, that define the logical encoding. The cat state $|\text{cat}_I^+\rangle_x$ only contains even parity levels and $|\text{cat}_I^-\rangle_x$

only contains odd parity levels, similar to bosonic cat states (23). In the basis $\{|I, m_I\rangle_z\}$ of the eigenstates of \hat{I}_z , corresponding to the physical quantization axis set by the nuclear Zeeman energy, the encoded states are given by

$$|\bar{0}\rangle = \sum_{m_I=-I}^I d_{m_I, -I}^I \left(\frac{\pi}{2}\right) |I, m_I\rangle_z, \quad (27)$$

$$|\bar{1}\rangle = \sum_{m_I=-I}^I d_{m_I, I}^I \left(\frac{\pi}{2}\right) |I, m_I\rangle_z, \quad (28)$$

where $d_{m', m}^I (\beta = \pi/2)$ is the Wigner d-function [16]. It is noteworthy that the codewords $|\bar{0}\rangle$ and $|\bar{1}\rangle$ for the spin-cat code are perfectly orthonormal to each other, unlike the bosonic cat code, which has $\mathcal{O}(\exp(-2|\alpha|^2))$ overlap between the encoded states.

B. Error correction

The physically dominant noise in spin systems arises from local fluctuations in the surrounding magnetic and electric fields, resulting in decoherence of the spins [17]. In particular, for a nuclear spin, errors along the physical quantization axis, i.e. the z axis, dominate over the errors along other axes, leading to a biased-noise system that could be used to reduce the overhead in fault tolerant quantum computation, similar to the bosonic case. The Schrödinger spin-cat code on a single high-spin nucleus can be used to correct biased errors that cause dephasing, described by the angular momentum operator \hat{I}_z . After an \hat{I}_z error, the nuclear spin state is given by

$$\hat{I}_z |\bar{0}\rangle = \hat{U}^\dagger (\hat{U} \hat{I}_z \hat{U}^\dagger) \hat{U} |I, -I\rangle_x = \hat{U}^\dagger \hat{I}_x |I, -I\rangle_z = \hat{U}^\dagger |I, -I+1\rangle_z = c_1 |I, -I+1\rangle_x, \quad (29)$$

$$\hat{I}_z |\bar{1}\rangle = \hat{U}^\dagger (\hat{U} \hat{I}_z \hat{U}^\dagger) \hat{U} |I, I\rangle_x = \hat{U}^\dagger \hat{I}_x |I, I\rangle_z = \hat{U}^\dagger |I, I-1\rangle_z = c_1 |I, I-1\rangle_x, \quad (30)$$

where c_1 is a complex number, $\hat{U} = e^{-i\frac{\pi}{2}\hat{I}_y}$ and $\hat{U} \hat{I}_z \hat{U}^\dagger = \hat{I}_x$. Similarly, after an \hat{I}_z^2 error, the encoded state is given by

$$\hat{I}_z^2 |\bar{0}\rangle = \hat{I}_z^2 |I, -I\rangle_x = c_2 |I, -I\rangle_x + c_3 |I, -I+2\rangle_x \quad (31)$$

$$\hat{I}_z^2 |\bar{1}\rangle = \hat{I}_z^2 |I, I\rangle_x = c_2 |I, I\rangle_x + c_3 |I, I-2\rangle_x, \quad (32)$$

where c_2 and c_3 are complex numbers. For spin $I \geq 5/2$, the codewords are orthogonal to each other for both linear and quadratic forms of the error \hat{I}_z , which can be corrected using the spin-cat code. In fact, a spin-7/2 cat code can also correct for \hat{I}_z^3 type errors, so, the set of correctable errors is spanned by $\{\mathbb{I}, \hat{I}_z, \hat{I}_z^2, \hat{I}_z^3\}$. The Schrödinger spin-cat code can exponentially suppress bit-flip errors as the spin I increases, with only a linear increase in phase-flip errors on the encoded qubit, similar to the bosonic-cat code.

C. Logical gates

Logical operations that process information encoded in a spin-cat qubit should preserve the noise bias, i.e.

$$\overline{U} \hat{E}_i \overline{U}^\dagger \propto \hat{E}_i, \quad (33)$$

where \hat{E}_i denotes the error operator and \overline{U} is a logical operation on the encoded qubit. Covariant π -rotations $\overline{U} = e^{i\pi\hat{I}_\alpha}$ about any axis $\alpha \in \{x, y, z\}$ satisfy this condition, and can be used to implement logical Pauli operations on the encoded qubit. In particular, the logical \overline{X} gate can be implemented by a covariant π -rotation about the z axis, which applies the transformation

$$e^{-i\pi\hat{I}_z} |\bar{0}\rangle = \sum_{m_I=-I}^I (-1)^{m_I} d_{m_I, -I}^I \left(\frac{\pi}{2}\right) |I, m_I\rangle_z \equiv |\bar{1}\rangle, \quad (34)$$

$$e^{-i\pi\hat{I}_z} |\bar{1}\rangle = \sum_{m_I=-I}^I (-1)^{m_I} d_{m_I, I}^I \left(\frac{\pi}{2}\right) |I, m_I\rangle_z \equiv |\bar{0}\rangle, \quad (35)$$

where we used Eq. (27) along with the relation $e^{-i\pi\hat{I}_z}|I, m_I\rangle_z = e^{-i\pi m_I}|I, m_I\rangle_z = (-1)^{m_I}|I, m_I\rangle_z$. Here, one can see that $e^{-i\pi\hat{I}_z}$ is equivalent to the logical Pauli gate \bar{X} . Similarly, the logical \bar{Z} gate can be implemented using a covariant π rotation about the x -axis leading to the transformation

$$e^{-i\pi\hat{I}_x}|\bar{0}\rangle = e^{-i\pi\hat{I}_x}|I, -I\rangle_x = (-1)^{-I}|I, -I\rangle_x \equiv |\bar{0}\rangle, \quad (36)$$

$$e^{-i\pi\hat{I}_x}|\bar{1}\rangle = e^{-i\pi\hat{I}_x}|I, I\rangle_x = (-1)^I|I, I\rangle_x \equiv -|\bar{1}\rangle, \quad (37)$$

where we used Eq. (27) along with the relation $e^{-i\pi\hat{I}_x}|I, m_I\rangle_x = e^{-i\pi m_I}|I, m_I\rangle_x$. It should be noted that the last equality only holds for half-odd integer spins. Thus, covariant rotations of the form $\bar{U} = e^{i\pi\hat{I}_\alpha}$ can be used to implement logical Pauli operations on the encoded state in bias-preserving way, allowing the Schrödinger spin-cat code to be concatenated with multi-qubit codes to achieve high-threshold fault tolerant quantum computation.

SI: 4. COVARIANT $SU(2)$ ROTATION THEORY

A. Generalised rotating frame

The dynamics of any system are relative to a specific frame of reference [18]. Quantum systems governed by their respective Hamiltonians are no exception. In the laboratory frame, the relative phase of a qubit accumulates at the resonance frequency determined by the energy difference between its two levels. However, one can define a rotating frame that counters this phase evolution, effectively altering the qubit's dynamics by transitioning to a different frame. Typically, the reference frequency of the rotating frame is selected to be equal to the qubit's resonance frequency, facilitating simpler dynamics within the rotating frame as the accumulating phase of the qubit is effectively cancelled out.

In higher-dimensional spin systems, the presence of multiple resonance frequencies means that no single reference frequency can cancel all relative phases between multiple energy levels. Nonetheless, the concept can be expanded to encompass a generalised rotating frame (GRF), which utilises multiple reference frequencies to account for different energy splittings between pairs of adjacent energy levels [19]. Here the GRF is tailored for an n -level non-degenerate quantum system, with each energy level labeled as E_i . The resonance frequencies of neighboring transitions are given by $f_i^0 = \frac{E_{i+1}-E_i}{\hbar}$, where \hbar is Planck's constant. We apply the generalised rotating frame transformation, which converts the Hamiltonian in the laboratory frame denoted as $\hat{\mathcal{H}}_{\text{lab}}$ into the Hamiltonian in the generalised rotating frame, $\hat{\mathcal{H}}_{\text{GRF}}$, through the unitary transformation:

$$\hat{\mathcal{H}}_{\text{GRF}} = \hat{\mathcal{U}}_{\text{GRF}}^\dagger \hat{\mathcal{H}}_{\text{lab}} \hat{\mathcal{U}}_{\text{GRF}} - i\hbar \hat{\mathcal{U}}_{\text{GRF}}^\dagger \frac{\partial \hat{\mathcal{U}}_{\text{GRF}}}{\partial t}, \quad (38)$$

where the unitary GRF operator $\hat{\mathcal{U}}_{\text{GRF}}$ is defined as

$$\hat{\mathcal{U}}_{\text{GRF}} = \begin{pmatrix} e^{-iE_1 t/\hbar} & 0 & 0 & 0 \\ 0 & e^{-iE_2 t/\hbar} & \dots & 0 \\ 0 & \vdots & \ddots & 0 \\ 0 & 0 & 0 & e^{-iE_n t/\hbar} \end{pmatrix}. \quad (39)$$

Within the GRF framework, $n-1$ distinct reference frequencies (f_i^{ref}) are required to fully counteract the $n-1$ resonance frequencies (f_i^0). Correspondingly, there are $n-1$ frequency detunings, denoted as $\delta_i = f_i^{\text{ref}} - f_i^0$. If the Hamiltonian is time-independent in the laboratory frame – in our case, in the absence of NMR driving terms – the GRF with zero detunings cancels it out completely, so that any state appears static within that frame.

B. Multi-frequency driving pulse

We now elucidate the system dynamics within the GRF framework when time-dependent driving terms are introduced. We confine our analysis to the ionised ^{123}Sb nuclear spin, but note that this concept is broadly applicable to various high-level systems.

In the laboratory frame, the time-dependent Hamiltonian of a high-spin system is expressed as follows:

$$\hat{\mathcal{H}}_{\text{lab}}(t) = \hat{\mathcal{H}}_{D^+} - \gamma_n \hat{I}_x \sum_{k=1}^{2I} \cos(2\pi f_k t + \phi_k) B_{1,k}(t), \quad (40)$$

where $\hat{\mathcal{H}}_{D^+}$ (Eq. (1) in the main text) is the static term of the ionised donor Hamiltonian, set by the Zeeman energy and the quadrupole interaction. In time-dependent term, f_k , ϕ_k , and $B_{1,k}(t)$ represent the frequency, phase, and amplitude of each tone in the driving pulse, respectively, and \hat{I}_x is the high spin operator along the x direction. For the spin-7/2 system,

$$\hat{I}_x^{7/2} = \frac{1}{2} \begin{pmatrix} 0 & \sqrt{7} & 0 & 0 & 0 & 0 & 0 & 0 \\ \sqrt{7} & 0 & \sqrt{12} & 0 & 0 & 0 & 0 & 0 \\ 0 & \sqrt{12} & 0 & \sqrt{15} & 0 & 0 & 0 & 0 \\ 0 & 0 & \sqrt{15} & 0 & \sqrt{16} & 0 & 0 & 0 \\ 0 & 0 & 0 & \sqrt{16} & 0 & \sqrt{15} & 0 & 0 \\ 0 & 0 & 0 & 0 & \sqrt{15} & 0 & \sqrt{12} & 0 \\ 0 & 0 & 0 & 0 & 0 & \sqrt{12} & 0 & \sqrt{7} \\ 0 & 0 & 0 & 0 & 0 & 0 & \sqrt{7} & 0 \end{pmatrix}. \quad (41)$$

Converting Eq. (40) into a time-independent Hamiltonian in the generalised rotating frame relies on two assumptions:

- Rotating wave approximation (RWA). The driving field in Eq. (40) can be decomposed into $2 \times 2I$ circular rotating fields with amplitude $B_{1,k}$ and with opposite rotating directions, represented by the frequencies f_k and $-f_k$. The RWA results in the reduction of $B_{1,k}$ by a factor of two by eliminating the counter-rotating terms with frequencies $-f_k$. The RWA is well obeyed in the present experiment, since the driving strength is intentionally set in the sub-kilohertz regime, making it $\sim 10,000\times$ smaller than the NMR frequencies, ≈ 7.7 MHz.
- Each tone k drives only a single transition, leaving all other states unaffected. This condition holds true when the driving strengths are much lower than the separations between resonance frequencies. With the increase of the driving strength, this assumption breaks down and the resulting Hamiltonian is detailed in Section SI: 4C. In our experiment, the frequency separation between each transition is determined by the quadrupole interaction (28 kHz), while the driving strength is set in the sub-kilohertz regime.

The resulting generalised rotating frame Hamiltonian has the form:

$$\hat{\mathcal{H}}_{\text{GRF}} = -\frac{\gamma_n}{4} \begin{pmatrix} 0 & \sqrt{7}B_{1,1}e^{i\phi_1} & 0 & 0 & 0 & 0 & 0 & 0 \\ \sqrt{7}B_{1,1}e^{-i\phi_1} & \delta_1 & \sqrt{12}B_{1,2}e^{i\phi_2} & 0 & 0 & 0 & 0 & 0 \\ 0 & \sqrt{12}B_{1,2}e^{-i\phi_2} & \delta_2 & \sqrt{15}B_{1,3}e^{i\phi_3} & 0 & 0 & 0 & 0 \\ 0 & 0 & \sqrt{15}B_{1,3}e^{-i\phi_3} & \delta_3 & \sqrt{16}B_{1,4}e^{i\phi_4} & 0 & 0 & 0 \\ 0 & 0 & 0 & \sqrt{16}B_{1,4}e^{-i\phi_4} & \delta_4 & \sqrt{15}B_{1,5}e^{i\phi_5} & 0 & 0 \\ 0 & 0 & 0 & 0 & \sqrt{15}B_{1,5}e^{-i\phi_5} & \delta_5 & \sqrt{12}B_{1,6}e^{i\phi_6} & 0 \\ 0 & 0 & 0 & 0 & 0 & \sqrt{12}B_{1,6}e^{-i\phi_6} & \delta_6 & \sqrt{7}B_{1,7}e^{i\phi_7} \\ 0 & 0 & 0 & 0 & 0 & 0 & \sqrt{7}B_{1,7}e^{-i\phi_7} & \delta_7 \end{pmatrix}. \quad (42)$$

In our implementation, a Quantum Machines OPX+, an FPGA-based signal generator, manages the amplitude $B_{1,k}$ of each tone, enabling individual tuning of the coupling strengths between energy levels. In addition, the signal generator creates the generalised rotating frame by defining 7 internal ‘virtual clocks’, i.e. 7 software-defined oscillators with a well-defined phase relationship with each other. With 14 independent parameters, $B_{1,k}$ and ϕ_k , this setup enables the covariant $SU(2)$ rotations of arbitrary angle Θ around an arbitrary equatorial axis φ within the GRF:

$$R_\Theta(\varphi) = e^{i\Theta(\hat{I}_x \cos \varphi + \hat{I}_y \sin \varphi)}. \quad (43)$$

Furthermore, manipulating the reference phases at the software level facilitates the virtual-SNAP gate (Supplementary Information, Section SI: 6). With these control capabilities, we can implement arbitrary axis covariant $SU(2)$ rotations, subspace rotations, and virtual-SNAP gate within the generalised rotating frame.

C. Power dependence of covariant $SU(2)$ rotations

The speed of covariant $SU(2)$ rotations is tunable by changing the amplitude of the oscillating magnetic fields, $B_{1,k}$, applied to the nucleus. In the experiment, we tune $B_{1,k}$ by changing the amplitude of the output of the FPGA signal generator, which drives a current through the on-chip broadband antenna [20] and generates the driving field. In Fig. S9a we show covariant Rabi oscillations for different output amplitudes of the source. By fitting a sinusoidal decay to each Rabi oscillation, we extract the Rabi frequency $f_{\text{Rabi}}^{\text{CR}}$ for each driving amplitude (Fig. S9b). We find a linear trend that is consistent with the expectation $f_{\text{Rabi}}^{\text{CR}} \propto B_{1,k}$.

Fig. S9a, however, shows that the fidelity of the covariant Rabi oscillations deteriorates at higher driving amplitudes, i.e. when the Rabi frequency $f_{\text{Rabi}}^{\text{CR}}$ approaches the value of the quadrupole splitting f_q^+ . The consequent power broadening results in a cross-talk between different nuclear transitions.

We determine the effect of power broadening by quantifying the decrease in contrast of the Rabi oscillations. We model cross talk by introducing the term $\zeta = 1 + e^{i\omega_q t} + e^{i2\omega_q t} + \dots + e^{i6\omega_q t}$, with $\omega_q = 2\pi f_q^+$, which includes the interaction due to the resonant driving tone, and the $n = 6$ off-resonant terms that are separated by multiples of the quadrupole shift f_q^+ . The driving Hamiltonian then yields

$$\hat{\mathcal{H}}(t) = -\frac{f_{\text{Rabi}}^{\text{CR}}}{2} \begin{pmatrix} 0 & \sqrt{7}\zeta & 0 & 0 & \dots & 0 \\ \sqrt{7}\zeta^* & 0 & \sqrt{12}e^{-i\omega_q t}\zeta & 0 & \dots & 0 \\ \vdots & & \ddots & & & \vdots \\ 0 & 0 & \dots & \sqrt{7}e^{-i6\omega_q t}\zeta^* & 0 \end{pmatrix}. \quad (44)$$

We solve the time evolution of the system under Eq. (44) starting from the state $| -7/2 \rangle$ using QuTiP [21]. We may solve either by directly integrating the time-dependent Schrödinger equation including these oscillatory terms, or perturbatively using average Hamiltonian theory, exploiting the fact that Eq. (44) is periodic with period $T = 1/f_q^+$. For the latter strategy, Floquet's theorem assures that the solution to the Schrödinger equation for this periodic Hamiltonian is $\hat{\mathcal{U}}_P(t) \exp(-i\hat{\mathcal{F}}t)$, where $\hat{\mathcal{U}}_P(t)$ is some perfectly periodic unitary (which resolves to identity every period), and $\hat{\mathcal{F}}$ is the Floquet hamiltonian, which we approximate via the Magnus expansion. In the regime $f_{\text{Rabi}}^{\text{CR}} < f_q^+$ and to first order, $\hat{\mathcal{F}} \approx \bar{\mathcal{H}}^{(0)} + \bar{\mathcal{H}}^{(1)}$ where

$$\bar{\mathcal{H}}^{(0)} = \frac{1}{T} \int_0^T dt_1 \hat{\mathcal{H}}(t_1) = \pi f_{\text{Rabi}}^{\text{CR}} \hat{I}_x, \quad (45)$$

$$\bar{\mathcal{H}}^{(1)} = \frac{-i}{2T} \int_0^T dt_2 \int_0^{t_2} dt_1 [\hat{\mathcal{H}}(t_1), \hat{\mathcal{H}}(t_2)]. \quad (46)$$

The first-order term $\bar{\mathcal{H}}^{(1)}$ is the correction to the simplest rotating-frame description of global Rabi driving given by $\bar{\mathcal{H}}^{(0)}$. For the example of our $I = 7/2$ system, this correction Hamiltonian evaluates to

$$\bar{\mathcal{H}}^{(1)} = \frac{(f_{\text{Rabi}}^{\text{CR}})^2}{16f_q^+} \begin{pmatrix} -\frac{343}{20} & 0 & -\sqrt{\frac{7}{3}} & 0 & 0 & 0 & 0 & 0 \\ 0 & \frac{7}{4} & 0 & -\frac{6}{\sqrt{5}} & 0 & 0 & 0 & 0 \\ -\sqrt{\frac{7}{3}} & 0 & \frac{133}{20} & 0 & -\sqrt{15} & 0 & 0 & 0 \\ 0 & -\frac{6}{\sqrt{5}} & 0 & \frac{35}{4} & 0 & -\sqrt{15} & 0 & 0 \\ 0 & 0 & -\sqrt{15} & 0 & \frac{35}{4} & 0 & -\frac{6}{\sqrt{5}} & 0 \\ 0 & 0 & 0 & -\sqrt{15} & 0 & \frac{133}{20} & 0 & -\sqrt{\frac{7}{3}} \\ 0 & 0 & 0 & 0 & -\frac{6}{\sqrt{5}} & 0 & \frac{7}{4} & 0 \\ 0 & 0 & 0 & 0 & 0 & -\sqrt{\frac{7}{3}} & 0 & -\frac{343}{20} \end{pmatrix}. \quad (47)$$

Relative to a the simple $SU(2)$ covariant rotation achieved by $\bar{\mathcal{H}}^{(0)}$, the correction from off-resonant terms causes an error scaling as $(f_{\text{Rabi}}^{\text{CR}}/f_q^+)^2$. This means that a covariant rotation will lose fidelity as either the power is increased, or as the quadrupolar splitting f_q^+ decreases. Of course, in the opposite extreme of the perturbative expansion, $f_{\text{Rabi}}^{\text{CR}} \gg f_q^+$, we enter the “hard-pulse” limit, in which a single-frequency broadband pulse can enact a $SU(2)$ rotation to all transitions, and once again covariant operations are possible. The intermediate regime, $f_{\text{Rabi}}^{\text{CR}} \approx f_q^+$ is poorly described by perturbation theory. It corresponds to the regime where chaotic dynamics takes place, i.e. where the spin behaves as the quantum version of a chaotic periodically-driven top [3].

Fig S9c shows the normalised maximum peak height $\max(\langle \hat{I}_z \rangle)/I$ of a covariant Rabi oscillation including off-resonant terms, both using the average Hamiltonian above or direct integration of the time-dependent Schrödinger equation. For very small Rabi frequencies, $f_{\text{Rabi}}^{\text{CR}} \ll f_q^+$, the effect is negligible and cross-coupling can be neglected. As $f_{\text{Rabi}}^{\text{CR}}/f_q^+$ grows, Rabi contrast decreases, and displays chaotic behaviour around $f_{\text{Rabi}}^{\text{CR}}/f_q^+ \approx 1$. After this regime, for $f_{\text{Rabi}}^{\text{CR}} \gg f_q^+$, covariant rotations are possible again as each frequency tone now drives all transitions. Our experiment operates at $f_{\text{Rabi}}^{\text{CR}}/f_q^+ \approx 10^{-2}$, where the error due to cross-coupling is on the order of $\approx 10^{-4}$. If desiring global rotations at stronger $f_{\text{Rabi}}^{\text{CR}}$ and an elimination of this error, an appropriate strategy would be RF pulse shaping, which has been used effectively in the past to enact desired operations in quadrupole-split nuclear systems [22].

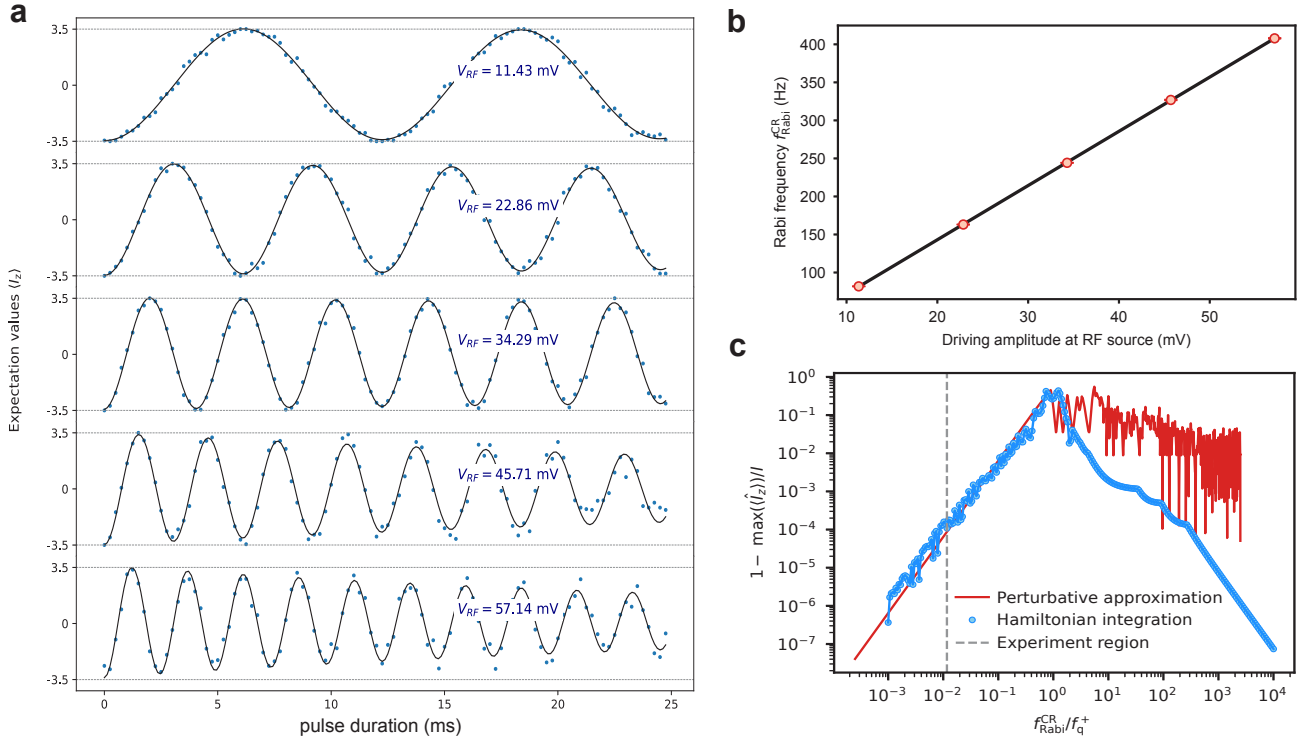


FIG. S9. **Dependence of covariant $SU(2)$ rotations on driving amplitude.** **a**, Spin expectation value, $\langle \hat{I}_z \rangle$, as a function of the RF pulse duration for 7 tones with equal amplitudes V_{RF} . Each expectation value is calculated from all 8 nuclear spin state probabilities, with each probability measured over 42 repetitions. The solid lines are exponentially-decaying sinusoidal fits to the measured data points. **b**, Rabi frequency $f_{\text{Rabi}}^{\text{CR}}$ extracted from the fits in **a** versus the RF driving amplitude V_{RF} . The error bars are derived from the fitting error, which are comparable to the symbol size. **c**, Numerically simulated error of covariant $SU(2)$ rotations as a ratio of Rabi frequency to quadrupole splitting. Blue data points are obtained via a time evolution of Eq. (44). The red line represents a perturbative approximation. The vertical dashed line represents the experimental setting used in the main text, where $V_{RF} = 22.86 \text{ mV}$.

SI: 5. SNAP GATES AND QUDIT UNIVERSALITY

We briefly review a proof of the fact that SNAP and covariant $SU(2)$ rotations unitaries are universal for control of a single qudit in any dimension. Independently, one can note that SNAP gates and Givens rotations ($SO(2)$'s) are also universal [23–25]. We utilize both facts in our experimental protocols. We refer to the Hilbert space dimension as $d = 2I + 1$, and since we work with a fixed total spin I , we will refer to the $|I, m_I\rangle$ states as $|m_I\rangle$ instead. With this notation, the SNAP gate is simply a diagonal unitary with arbitrary phases on each diagonal (inspired from the analogous quantity in cavity-QED systems [25, 26]),

$$\hat{S}(\vec{\xi}) = \sum_{m=1}^d e^{i\xi_m} |m_I\rangle \langle m_I|, \quad (48)$$

where $\vec{\xi} = (\xi_1, \xi_2, \dots, \xi_d)$ is the vector of phases. Occasionally we will need to use the “linear SNAP”, $(\hat{\mathcal{S}}(\varphi) = \sum_{m_I=1}^d e^{im_I\varphi} |m_I\rangle\langle m_I|)$. We call this a linear SNAP because of the linear relationship between the phases on the diagonal, $\xi_{m_I} = m_I\varphi \ \forall m_I \in \{1, 2, \dots, d\}$. We first note that the covariant $SU(2)$ rotation along θ, φ can be obtained by a purely θ rotation and SNAP gates:

$$\hat{\mathcal{D}}(\theta, \varphi) = \hat{\mathcal{S}}(\varphi)\hat{\mathcal{D}}(\theta, 0)\hat{\mathcal{S}}^\dagger(\varphi), \quad (49)$$

where $\mathcal{S}(\varphi)$ is the linear SNAP gate defined above. Moreover, notice that since, $\hat{\mathcal{D}}(\theta, 0) = \exp\left[\frac{\theta}{2}(\hat{I}_- - \hat{I}_+)\right]$ and $\hat{I}_- - \hat{I}_+ = -2i\hat{I}_y$, we have, $\hat{\mathcal{D}}(\theta, 0) = e^{-i\theta\hat{I}_y}$. That is, displacements by a θ direction only correspond to a \hat{I}_y rotation with the same angle (up to a minus sign). Putting these together, we have,

$$\hat{\mathcal{D}}(\theta, \varphi) = \hat{\mathcal{S}}(\varphi) \exp\left[-i\theta\hat{I}_y\right] \hat{\mathcal{S}}^\dagger(\varphi). \quad (50)$$

That is, a covariant $SU(2)$ rotation of (θ, φ) can be generated from linear SNAP gates with angle φ and a \hat{I}_y rotation only.

The proof of universality of SNAP and displacements follows closely that of Ref. [25]. In fact, our proof is even simpler since we are working with a single finite-dimensional Hilbert space (see also [27] for some recent work on deciding universality of discrete gate sets via Lie algebraic techniques). We will only focus on rotations generated by $\hat{\mathcal{D}}(\theta, 0) = \exp[-i\theta\hat{I}_y]$ with $\theta \in [0, \pi]$ (since the φ part can be obtained via SNAP gates). Let $\hat{\Gamma}_n = \sum_{j=0}^n |j\rangle\langle j|$ be the projector onto the first n levels. Then, it is easy to show that two-level rotations can be obtained as,

$$\hat{\mathcal{R}}_n := -i\left[\hat{I}_y, \hat{\Gamma}_n\right] \propto (|n\rangle\langle n+1| + |n+1\rangle\langle n|), \quad (51)$$

where $\hat{\mathcal{R}}_n$ is the generator of $SO(2)$ rotations between levels $|n\rangle$ and $|n+1\rangle$. Therefore, using $\hat{\mathcal{R}}_n$ and $\hat{\Gamma}_n$ we can generate the Lie algebra $u(d)$ and hence generate any Hamiltonian evolution for the qudit, proving the universality of SNAP and covariant $SU(2)$ rotations operations.

Moreover, similar to [25], let $\hat{\mathcal{U}}_n(\epsilon) := e^{i\epsilon\hat{\Gamma}_n} = \sum_{j=0}^n e^{i\epsilon}|j\rangle\langle j|$ be an infinitesimal rotation of all the levels, then alternating these “pulses” generates, up to second order in ϵ the two-level rotation. That is,

$$\hat{\mathcal{D}}(\epsilon)\hat{\mathcal{U}}_n(\epsilon)\hat{\mathcal{D}}(-\epsilon)\hat{\mathcal{U}}_n(-\epsilon) = \exp\left(i\hat{\mathcal{R}}_n\epsilon^2 + \mathcal{O}(\epsilon^3)\right). \quad (52)$$

This combined with the fact that we can compile any $d \times d$ unitary into $O(d^2)$ SNAPS and $SO(2)$ rotations (also known as Givens rotations) [23–25] allows for an (in-principle) protocol to implement any single qudit unitary gate.

SI: 6. CREATION OF SPIN CAT STATES WITH VIRTUAL-SNAP GATE

A. Arbitrary virtual-SNAP gates on the nuclear spin

The SNAP gate originates from work in microwave oscillators, where an ancilla transmon qubit is used to introduce arbitrary phases to the oscillator’s Fock states by performing transmon rotations that create a tunable geometric phase [26]. Our work differs from such setup in two important ways: (i) our system is intrinsically nonlinear (anharmonic) due to the nuclear quadrupole coupling, so we do not need to employ an ancilla qubit for state-selective operations, and (ii) we perform the SNAP gate virtually, by updating the phase of the GRF. This update is realized by a software instruction to shift by $\Delta\phi_k$ the phases of the 7 internal clocks in the Quantum Machines OPX+ signal generator. The driving terms in the laboratory frame Hamiltonian (Eq. (40)) transform into: $B_{1,k} \cos(2\pi f_k t + \phi_k + \Delta\phi_k)$, which adds a phase shift to the off-diagonal terms in the generalised rotating frame Hamiltonian (for brevity, we set all initial ϕ_k to 0):

$$\hat{\mathcal{H}}_{\text{update}}(\Delta\phi) = \frac{-\gamma_n}{4} \begin{pmatrix} 0 & \sqrt{7}B_{1,1}e^{i\Delta\phi_1} & 0 & \cdots & 0 & 0 \\ \sqrt{7}B_{1,1}e^{-i\Delta\phi_1} & 0 & \sqrt{12}B_{1,2}e^{i\Delta\phi_2} & \cdots & 0 & 0 \\ 0 & \sqrt{12}B_{1,2}e^{-i\Delta\phi_2} & 0 & \cdots & 0 & 0 \\ \vdots & \vdots & \vdots & \ddots & \vdots & \vdots \\ 0 & 0 & 0 & \cdots & 0 & \sqrt{7}B_{1,7}e^{i\Delta\phi_7} \\ 0 & 0 & 0 & \cdots & \sqrt{7}B_{1,7}e^{-i\Delta\phi_7} & 0 \end{pmatrix}, \quad (53)$$

where $\hat{\mathcal{H}}_{\text{update}}$ denotes the Hamiltonian after the frame update and $\Delta\phi = (\Delta\phi_1, \Delta\phi_2, \dots, \Delta\phi_7)$ are the applied phase shifts to each of the 7 internal clocks. The question is now: what unitary has been applied to the state of the nucleus in the generalised rotating frame as a result of the frame rotation? We can see that in the interaction picture, the frame rotation transforms $\hat{\mathcal{H}}_{\text{GRF}}$ as follows:

$$\hat{\mathcal{H}}_{\text{update}}(\Delta\phi) = \hat{\mathcal{S}}\hat{\mathcal{H}}_{\text{GRF}}\hat{\mathcal{S}}^\dagger, \quad (54)$$

where $\hat{\mathcal{S}}$ denotes the unitary SNAP gate for spin-7/2:

$$\hat{\mathcal{S}} = \begin{pmatrix} 1 & 0 & 0 & 0 & 0 & 0 & 0 & 0 \\ 0 & e^{i\xi_1} & 0 & 0 & 0 & 0 & 0 & 0 \\ 0 & 0 & e^{i\xi_2} & 0 & 0 & 0 & 0 & 0 \\ 0 & 0 & 0 & e^{i\xi_3} & 0 & 0 & 0 & 0 \\ 0 & 0 & 0 & 0 & e^{i\xi_4} & 0 & 0 & 0 \\ 0 & 0 & 0 & 0 & 0 & e^{i\xi_5} & 0 & 0 \\ 0 & 0 & 0 & 0 & 0 & 0 & e^{i\xi_6} & 0 \\ 0 & 0 & 0 & 0 & 0 & 0 & 0 & e^{i\xi_7} \end{pmatrix}. \quad (55)$$

We can now express the phase gate angles ξ_k into the frame rotation angles $\Delta\phi_k$ as:

$$\xi_k = -\sum_{i=1}^k \Delta\phi_i. \quad (56)$$

This relationship demonstrates that the phase acquired on the \hat{I}_z eigenstate $|k - 7/2\rangle$ is the cumulative sum of the frame update angles from $\Delta\phi_1$ to $\Delta\phi_k$. This approach provides a straightforward and nearly instantaneous (within a single clock cycle of the OPX+, 4 ns) method to implement a SNAP gate. Although it's easiest to recognize the effect of the frame update by writing it in terms of the driving Hamiltonian, this SNAP gate is *virtual* because it does not require any signal to be physically applied to the nucleus.

B. Implementation of one-axis twisting by virtual-SNAP

The second-order nonlinearity, \hat{I}_z^2 , in the Hamiltonian (Eq. 1 of the main text) introduces one-axis twisting of the spin state, a widely studied phenomenon in the context of spin squeezing [28]. In the laboratory frame, the one-axis twisting dynamics can induce the revival and collapse between the Schrödinger cat state and the spin coherent state lying on the equatorial plane of the Bloch sphere [29]. An appealing way to conceptualise the ability of the virtual-SNAP gate to suddenly transform a spin coherent state into a cat state is by realising that such transformation happens anyway, periodically, in the laboratory frame. The initial $|\text{scs}_{7/2}\rangle_x$ state only appears static because we have 'locked' onto it through the definition of the GRF. By switching to a different set of GRF phases through the virtual-SNAP, we suddenly 'lock' to a different point along the collapse-revival dynamics that takes place in the lab frame, and we choose that point to be the one where a cat state is formed.

In particular,

$$R_{\pi/2}(0)e^{-i\hat{I}_z^2\pi/2}R_{\pi/2}(-\pi/2) \equiv \frac{1}{\sqrt{2}} \begin{pmatrix} 1 & 0 & 0 & 0 & 0 & 0 & 0 & i \\ 0 & -i & 0 & 0 & 0 & 0 & 1 & 0 \\ 0 & 0 & 1 & 0 & 0 & i & 0 & 0 \\ 0 & 0 & 0 & -i & 1 & 0 & 0 & 0 \\ 0 & 0 & 0 & i & 1 & 0 & 0 & 0 \\ 0 & 0 & 1 & 0 & 0 & -i & 0 & 0 \\ 0 & i & 0 & 0 & 0 & 0 & 1 & 0 \\ 1 & 0 & 0 & 0 & 0 & 0 & 0 & -i \end{pmatrix}, \quad (57)$$

with equivalence up to virtual-SNAPs, which clearly enables the construction of cat-states in any subspace using covariant rotations and \hat{I}_z^2 evolution only. Given the fact that \hat{I}_z^2 exclusively modifies phases while leaving state population unaffected, we are able to utilise the virtual-SNAP gate to implement the one-axis twisting by adjusting phases in the generalised rotating frame. However, it should be noted that by using the virtual-SNAP gate, one can only generate certain equatorial cat states – those with identical populations to spin coherent state along the equator.

In practice, we perform a covariant $SU(2)$ rotation to the initial eigenstate $| -7/2 \rangle$ to first prepare the coherent state $| \text{scs}_{7/2} \rangle_x$, and then apply $\hat{\mathcal{S}}_{\text{cat}}$ to create an x -oriented Schrödinger cat state $| \text{cat}_{7/2}, \xi_7 = \pi/2 \rangle_x$, with the form:

$$| \text{scs}_{7/2} \rangle_x = \begin{pmatrix} -0.088 \\ 0.234 \\ -0.405 \\ 0.523 \\ -0.523 \\ 0.405 \\ -0.234 \\ 0.088 \end{pmatrix}, \quad (58a) \quad | \text{cat}_{7/2}, \xi_7 = \pi/2 \rangle_x = \begin{pmatrix} -0.088 \times e^{-i\frac{3\pi}{4}} \\ 0.234 \times e^{-i\frac{\pi}{4}} \\ -0.405 \times e^{-i\frac{3\pi}{4}} \\ 0.523 \times e^{-i\frac{\pi}{4}} \\ -0.523 \times e^{-i\frac{3\pi}{4}} \\ 0.405 \times e^{-i\frac{\pi}{4}} \\ -0.234 \times e^{-i\frac{3\pi}{4}} \\ 0.088 \times e^{-i\frac{\pi}{4}} \end{pmatrix}. \quad (58b)$$

It is clear that $\hat{\mathcal{S}}_{\text{cat}}$ with the following form is able to induce the transition from $| \text{scs}_{7/2} \rangle_x$ to $| \text{cat}_{7/2}, \xi_7 = \pi/2 \rangle_x$:

$$\hat{\mathcal{S}}_{\text{cat}} = e^{-i\frac{3\pi}{4}} \begin{pmatrix} 1 & 0 & 0 & 0 & 0 & 0 & 0 & 0 \\ 0 & e^{i\frac{\pi}{2}} & 0 & 0 & 0 & 0 & 0 & 0 \\ 0 & 0 & 1 & 0 & 0 & 0 & 0 & 0 \\ 0 & 0 & 0 & e^{i\frac{\pi}{2}} & 0 & 0 & 0 & 0 \\ 0 & 0 & 0 & 0 & 1 & 0 & 0 & 0 \\ 0 & 0 & 0 & 0 & 0 & e^{i\frac{\pi}{2}} & 0 & 0 \\ 0 & 0 & 0 & 0 & 0 & 0 & 1 & 0 \\ 0 & 0 & 0 & 0 & 0 & 0 & 0 & e^{i\frac{\pi}{2}} \end{pmatrix}. \quad (59)$$

Based upon Eq. (56), this $\hat{\mathcal{S}}_{\text{cat}}$ gate can be in practice achieved in the GRF with a software instruction to update:

$$\Delta\phi = (-\pi/2, +\pi/2, -\pi/2, +\pi/2, -\pi/2, +\pi/2, -\pi/2) \quad (60)$$

The method of applying alternating phases of $-\pi/2$ and $\pi/2$ is applicable more generally to create zero-parity $| \text{cat}_I \rangle_x$ for all half-odd integer spins. We thus employ this method to create subspace cats ($| \text{cat}_{5/2} \rangle_x, | \text{cat}_{3/2} \rangle_x$) as illustrated in Fig. 4e of the main text.

SI: 7. SUBSPACE ROTATIONS AND DIFFERENT SIZE CAT STATES

In the nuclear spin-7/2 system, it is possible to restrict the full 8-dimensional Hilbert space to specific subspaces, thereby simulating spins of varying sizes. For example, by constraining to the subspace spanned by $\{| 3/2 \rangle, | 1/2 \rangle, | -1/2 \rangle, | -3/2 \rangle\}$, we effectively emulate a spin-3/2 system.

The covariant $SU(2)$ rotations in the subspace require adjusting the driving amplitude, $B_{1,k}$, of each tone. One must ensure that the driving strength, determined by $B_{1,k}$ and the element of the spin-7/2 operator $\hat{I}_x^{7/2}$, matches the spin operator in the subspace. For instance, one can implement a spin-3/2 covariant rotation by matching $\sqrt{15}B_{1,3}$, $\sqrt{16}B_{1,4}$, and $\sqrt{15}B_{1,5}$, to the corresponding off-diagonal elements in the spin-3/2 $\hat{I}_x^{3/2}$ operator, while all other $B_{1,k}$ are set to zero. The corresponding spin operator $\hat{I}_x^{3/2}$ for the spin-3/2 system has the form:

$$\hat{I}_x^{3/2} = \frac{1}{2} \begin{pmatrix} 0 & \sqrt{3} & 0 & 0 \\ \sqrt{3} & 0 & 2 & 0 \\ 0 & 2 & 0 & \sqrt{3} \\ 0 & 0 & \sqrt{3} & 0 \end{pmatrix}. \quad (61)$$

The experimental demonstration of subspace covariant $SU(2)$ rotations is shown in Fig. S10. We initialise the spin in the \hat{I}_z eigenstate with the highest energy, e.g. $| -7/2 \rangle$ for a spin-7/2 subspace, $| -3/2 \rangle$ for the spin-3/2 subspace. A multi-frequency NMR pulse is applied with the power of each tone adjusted to implement a subspace rotation. For each subspace, the $\langle \hat{I}_z \rangle$ expectation value shows a sinusoidal oscillation with an amplitude that corresponds to the size of the subspace. From these oscillations, we extract the Rabi frequency of the subspace covariant $SU(2)$ rotation via a sinusoidal fit. As the total power is held constant, the Rabi frequency increases as the subspace gets smaller. We then use the Rabi frequency to numerically simulate an ideal subspace rotation around the $-y$ -axis and find excellent agreement with our data.

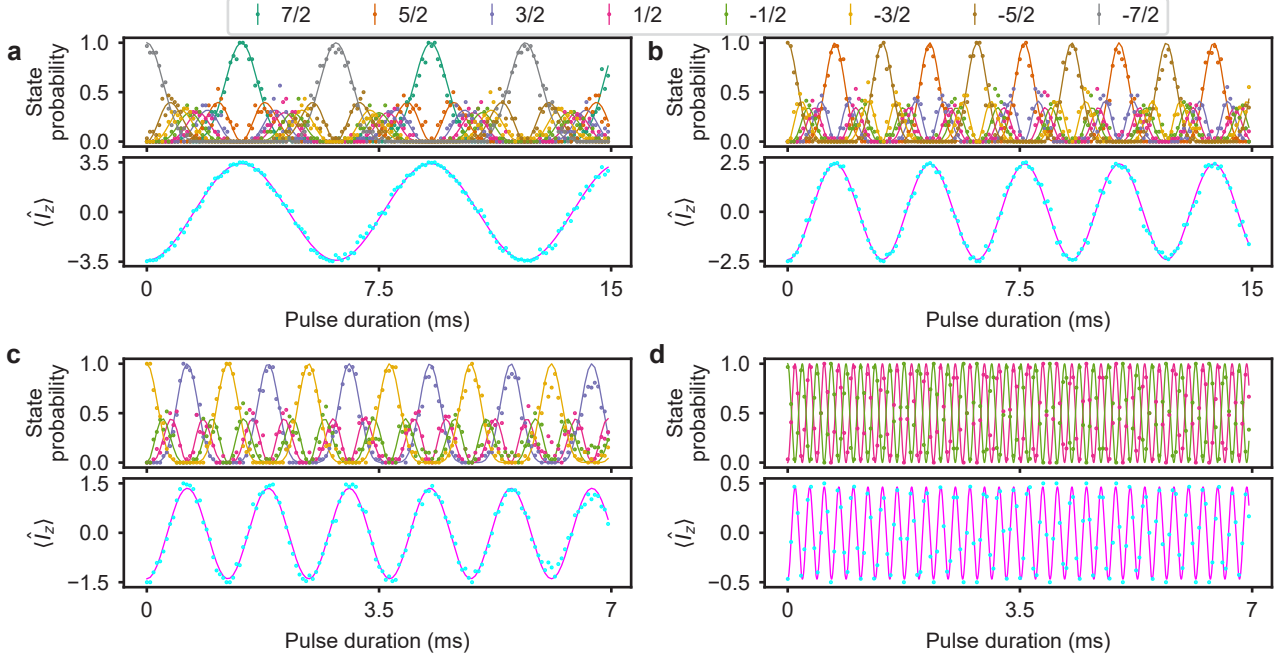


FIG. S10. **Subspace covariant $SU(2)$ rotations.** Subspaces with sizes **a** $I = 7/2$, **b** $I = 5/2$, **c** $I = 3/2$, **d** $I = 1/2$. Each panel shows the evolution of the state probabilities (top) and of the $\langle \hat{I}_z \rangle$ expectation values (bottom). Cyan points show $\langle \hat{I}_z \rangle$ expectation values calculated from the state probabilities. Solid magenta lines show a sinusoidal fit to extract the Rabi frequency.

Fig. S11 illustrates the Wigner functions of spin Schrödinger cat states within subspaces of dimensions $d=8, 6, 4$, and 2 (the $d=2$ case is not a cat state by any sensible definition, but we show it here to illustrate the universality of the operations), with corresponding density matrices and parity oscillations. The different-sized cat states are created using the Givens rotations protocol outlined in Fig. 3a-b of the main text. Subsequently, we perform density matrix tomography using the method described in Section SI: 9. Fig. S11a shows the absolute value of the density matrix of cat states in four different subspaces, sorted in descending order by size. Fig. S11b shows the Wigner function of the reconstructed density matrix in the full 8-dimensional Hilbert space. To highlight the cat-like features of the produced states, we truncate and normalize the reconstructed density matrix and plot the Wigner function of the resulting reduced density matrix in Fig. S11c. It becomes clear that the number of peaks and valleys in the Wigner function scales with the dimension of the cat state. For instance, in the spin- $7/2$ cat, there are 7 valleys; in the spin- $5/2$ cat, there are 5 valleys, and so on. This scaling is also reflected in Fig. S11d, where we display the parity oscillations of the different size cat state using the same method as in Fig. 3 of the main text. The number of periods of a cat state spanning d dimensions is $d-1$. The appearance of Wigner function negativity even in the trivial spin- $1/2$ case may seem surprising at first sight, but it reflects the fact that even Gaussian-like spin coherent states (which all pure spin- $1/2$ states are forced to be [28]) have Wigner negativity [30], unless $I \rightarrow \infty$.

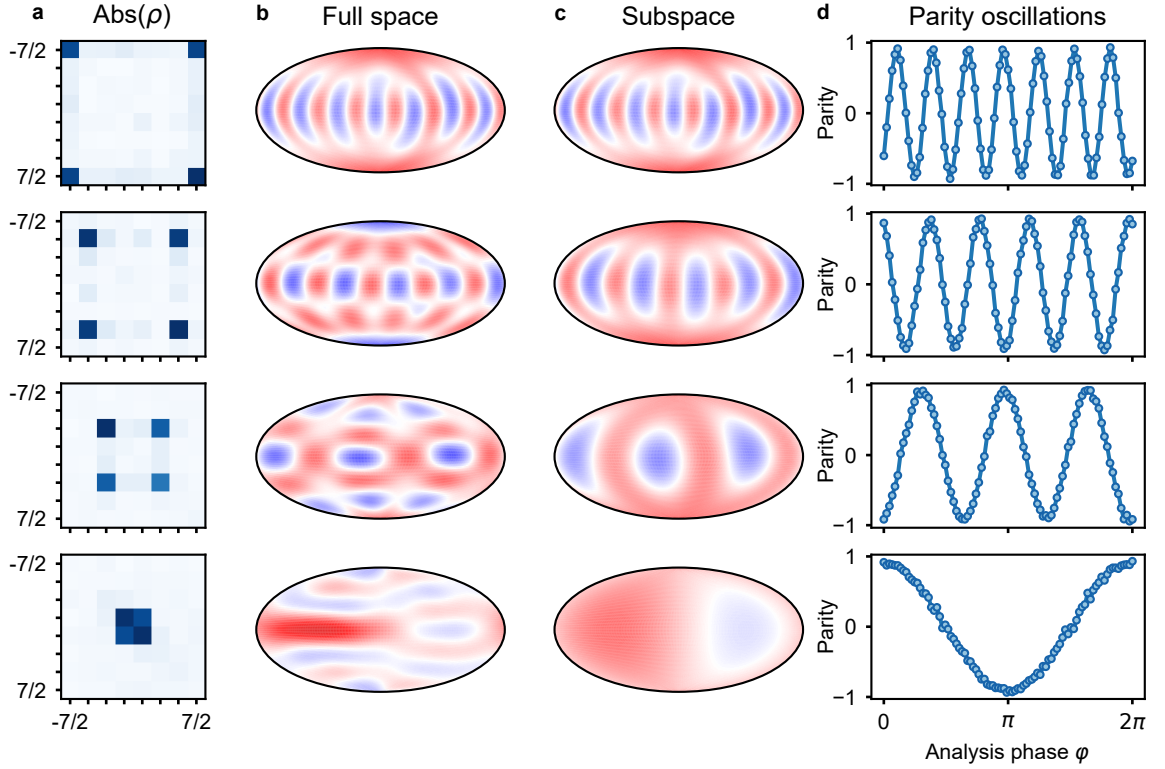


FIG. S11. **Full and subspace Schrödinger cat states in the $I = 7/2$ nuclear spin system.** Visualisation of density matrix reconstruction and parity oscillations for cat states across dimensions $d = 8$ (top row), 6 (second row), 4 (third row), and 2 (bottom row). The panels depict: **a**, absolute value of the density matrix, **b**, Wigner function in the 8-dimensional Hilbert space, **c**, Wigner function of the truncated density matrix highlighting cat-like properties, and **d**, parity oscillations, showing $d - 1$ periods. Each parity of the state is measured over 750 repetitions and error bars are smaller than the symbol size.

SI: 8. PARITY MEASUREMENT

In order to determine the coherence and fidelity of the $|{\text{cat}_{7/2}}_z\rangle$ state, we use a reduced tomography method based on measuring parity oscillations [31]. The state created in the experiment is described by the density matrix, ρ , with elements $\rho_{i,j}$, where i, j denote the m_I spin projections onto the z -axis. The fidelity, \mathcal{F} , between ρ and the cat state $|{\text{cat}_{7/2}}_z\rangle = (|7/2\rangle + e^{i\xi_7} |{-7/2}\rangle)/\sqrt{2}$ is given by

$$\mathcal{F} = {}_z \langle {\text{cat}_{7/2}} | \rho | {\text{cat}_{7/2}} \rangle_z = \frac{1}{2} (\rho_{-7/2, -7/2} + \rho_{7/2, 7/2}) + \frac{1}{2} (e^{i\xi_7} \rho_{-7/2, 7/2} + \text{c.c.}), \quad (62)$$

where the first term corresponds to the sum of the state probabilities of $|{-7/2}\rangle$ and $|7/2\rangle$, and the second term to the sum of the coherences. The state probabilities are determined with a projective measurement in the \hat{I}_z basis, while the coherences are determined by rotating the $|{\text{cat}_{7/2}}_z\rangle$ state to the equator of the spin sphere by applying a covariant $SU(2)$ rotation, $R_{\pi/2}(\varphi)$.

We then evaluate the parity operator $\hat{\Pi} = \sum_{m_I} (-1)^{I+m_I} |m_I\rangle \langle m_I|$ as a function of φ and find

$$\langle \hat{\Pi}(\varphi) \rangle = \frac{1}{2} \sum_{m_I} (-1)^{I+m_I} (e^{i2m_I\varphi} \rho_{m_I, -m_I} - e^{-i2m_I\varphi} \rho_{-m_I, m_I}), \quad (63)$$

which describes a sum of sinusoidal oscillations with periods $2\pi/7, 2\pi/5, 2\pi/3, 2\pi$ and amplitudes depending on the absolute value of the coherences. For the $|{\text{cat}_{7/2}}_z\rangle$ state prepared in the experiment, we find $\rho_{\pm 7/2, \pm 7/2} \gg \rho_{i,i}$ with $i = \pm 5/2, \pm 3/2, \pm 1/2$ and can therefore neglect the oscillations with periods $> 2\pi/7$ as we expect the coherences between the unpopulated states to be zero. The remaining oscillation that we observe in the experiment (see main text Fig. 2c,g) is then dominated by the term ($e^{i7\varphi}\rho_{-7/2,7/2} + \text{c.c.}$), which corresponds to the second term of Eq. (62). Hence, the state fidelity can then be computed by averaging the state populations and the contrast of the parity oscillation. In addition, the phase offset of the parity oscillation gives information about the phase ξ_7 of the state.

SI: 9. DENSITY MATRIX RECONSTRUCTION

It is *possible* to estimate the Wigner function $W(\theta, \varphi)$ of a large spin by measuring it directly at a dense grid of points (θ_n, φ_n) , expressing $W(\theta, \varphi)$ in terms of the outcome probabilities of a spin measurement in the (θ_n, φ_n) direction [32]. However, a much more efficient protocol is to estimate the Wigner function by using Eq. (20) to relate $W(\theta, \varphi)$ to a $(2I+1) \times (2I+1)$ density matrix ρ . Unlike $W(\theta, \varphi)$, which is defined at uncountably many points, ρ is described by just $4I(I+1)$ numbers, and can be estimated using quantum state tomography [33]. We do so, and then compute $W_\rho(\theta, \varphi)$ at all points using the tomographic estimate ρ_{MLE} .

A. Tomographic measurement protocol

At least $2I+2$ different quantum measurement bases are required for tomography. Each basis measurement has $2I+1$ distinct outcomes whose probabilities yield $2I$ independent real numbers, so $2I(2I+2) = 4I(I+1)$ density matrix elements can be deduced. The measurements we can make easily are measurements of $\hat{\mathbf{I}} \cdot \mathbf{n}$, where $\mathbf{n} \sim (\theta, \varphi)$ is a unit vector. Because $\hat{\mathbf{I}} \cdot \mathbf{n}$ measurements are not entirely uncorrelated with each other, measuring along $2I+2$ axes is not sufficient. Instead, $4I+1$ are both necessary [34] and sufficient [35]. For our spin- $7/2$ system, $4I+1 = 15$. But achieving optimal efficiency (accuracy vs number of samples) does not appear to be possible with a minimal set of $4I+1$ measurements [36].

The tomographic efficiency of a particular set of measurements (a.k.a. *experiment design*) is determined by the condition number of the *frame superoperator* whose action on a state ρ is

$$F[\rho] = \frac{1}{N} \sum_{j=1}^N E_j \text{Tr}[E_j], \quad (64)$$

where E_j denotes an *effect* of a measurement (i.e., the projector $|m_{\theta_n, \varphi_n}\rangle\langle m_{\theta_n, \varphi_n}|$ onto an eigenstate of $\hat{\mathbf{I}} \cdot \mathbf{n}_{\theta_n, \varphi_n}$), and ranges over all N effects in the experiment design (every effect of every measurement performed). If F is rank-deficient, then the experiment design is not *informationally complete*, and precise tomography is impossible. A good experimental design is one for which the spectrum of F is as flat as possible, and has no small eigenvalues. A good metric for quantifying tomographic efficiency is

$$f_{\text{te}}(F) = \sqrt{\text{Tr}(F^{-1})}, \quad (65)$$

with *smaller* f_{te} being better. The best possible tomographic efficiency for $I = 7/2$, achieved by a 2-design [37], is $f_{\text{te}} = \sqrt{4545} \approx 67.41$.

Among experiment designs comprised entirely of $\hat{\mathbf{I}} \cdot \mathbf{n}$ measurements, the best performance is achieved by measuring *all* axes according to a spherically uniform distribution ($f_{\text{te}} = \sqrt{5440} \approx 73.76$). This is obviously impossible in an experiment, since there are infinitely many axes. We used numerical analysis to find a small experiment design comprising just $45 = 3 \times 15$ measurement axes whose efficiency is very close to optimal ($f_{\text{te}} \approx 76.3$). This experiment design comprises a grid over (θ, φ) , with 15 equally spaced values of $\varphi_n = n \frac{2\pi}{15}$ ($n = 0 \dots 14$), and 3 specific values of $\theta_n = \{\frac{\pi}{4}, \frac{\pi}{3}, \frac{9\pi}{20}\}$, where $\theta = 0$ indicates the sphere's axis and $\theta = \pi/2$ its equator.

We used this experiment design for all state reconstructions. In most cases, we performed 15 shots of each measurement, for a total of $15 \times 45 = 675$ shots. In one case we performed 50 shots of each measurement, and in two cases we performed 80 shots.

B. Maximum likelihood state estimation

For each state that we reconstructed, we recorded all the data (outcomes of each shot), and then used unmodified maximum likelihood estimation (MLE) [33] to obtain an estimate ρ_{MLE} of the density matrix. The data form a list

$\{(E_j, n_j)\}$ of effects ($E_j = |m_{\theta_j, \varphi_j}\rangle \langle m_{\theta_j, \varphi_j}|$) and their observed frequencies (n_j). The MLE is obtained by constructing the *likelihood function*,

$$\mathcal{L}(\rho) \equiv \Pr(\text{data}|\rho) = \prod_j \text{Tr}(E_j \rho)^{n_j}, \quad (66)$$

and then finding its maximum over all ρ satisfying $\rho \geq 0$ and $\text{Tr}\rho = 1$. In practice, we minimize the negative *loglikelihood* $-\log(\mathcal{L})$ because it is convex.

We implemented this method with CVXPY 1.4 as a modeling platform and MOSEK 10 as a numerical solver [38, 39]. Specifically, letting \mathbf{Es} denote a matrix whose rows are obtained by flattening each E_j in row-major order, and letting \mathbf{ns} denote a corresponding vector of observed frequencies, the MLE is obtained as follows:

```
import cvxpy as cp
rho = cp.Variable(shape=(8, 8), hermitian=True)
probs = cp.real(Es @ rho.flatten(order='C'))
loglikelihood = cp.sum(cp.multiply(ns, cp.log(probs)))
objective = cp.Maximize(loglikelihood)
problem = cp.Problem(objective, [rho >> 0, cp.trace(rho) == 1])
problem.solve(solver='MOSEK')
rho_MLE = rho.value
```

We ran this code on many different datasets (both real and simulated) and found that it took between 0.1 and 0.2 seconds to execute on a MacBook Pro with an M2 Max processor. Notably, this is less than the time required just to compute the eigenstates of $\hat{\mathbf{I}} \cdot \mathbf{n}_{\theta_n, \varphi_n}$ by standard numerical methods. Therefore for improved efficiency we computed these eigenstates by leveraging a symbolic eigendecomposition of $\hat{\mathbf{I}} \cdot \mathbf{n}_{\theta_n, \varphi_n}$ obtained with Maple.

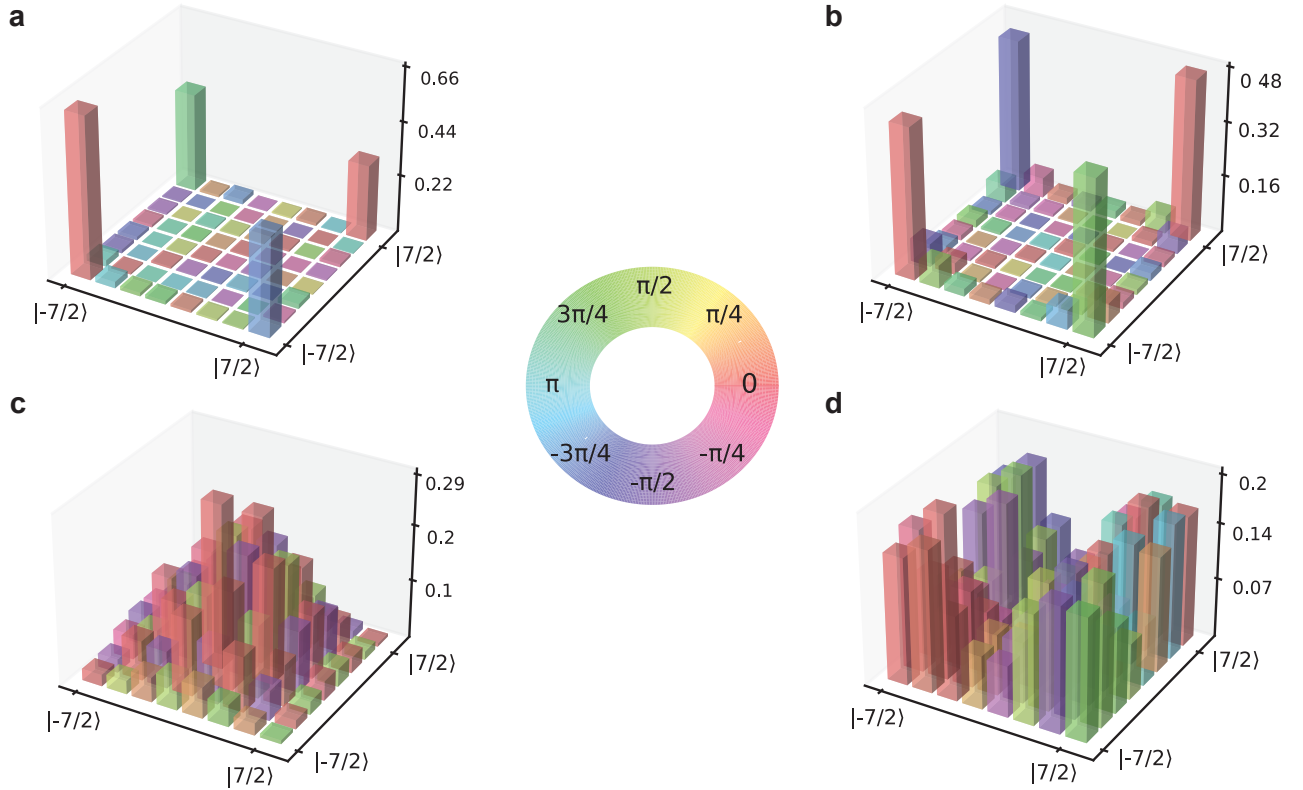


FIG. S12. **Reconstructed density matrices of the spin cat states.** **a**, $|\text{cat}_{7/2}, \xi_7 = -\pi\rangle_z = (| -7/2 \rangle - | 7/2 \rangle)/\sqrt{2}$, prepared by Givens rotations. **b**, $|\text{cat}_{7/2}, \xi_7 = \pi/2\rangle_z = (| -7/2 \rangle + i| 7/2 \rangle)/\sqrt{2}$, prepared by the sequence of $\pi/2$ covariant $SU(2)$ rotation + virtual-SNAP + $\pi/2$ covariant $SU(2)$ rotation. **c**, $|\text{cat}_{7/2}, \xi_7 = \pi/2\rangle_x$, prepared by the sequence of $\pi/2$ covariant $SU(2)$ rotation + virtual-SNAP. **d** Cat state obtained after a $\pi/4$ covariant $SU(2)$ rotation of $|\text{cat}_{7/2}, \xi_7 = \pi/2\rangle_x$, i.e. the second-last example depicted in the Hammer projection of Fig. 3h of the main text.

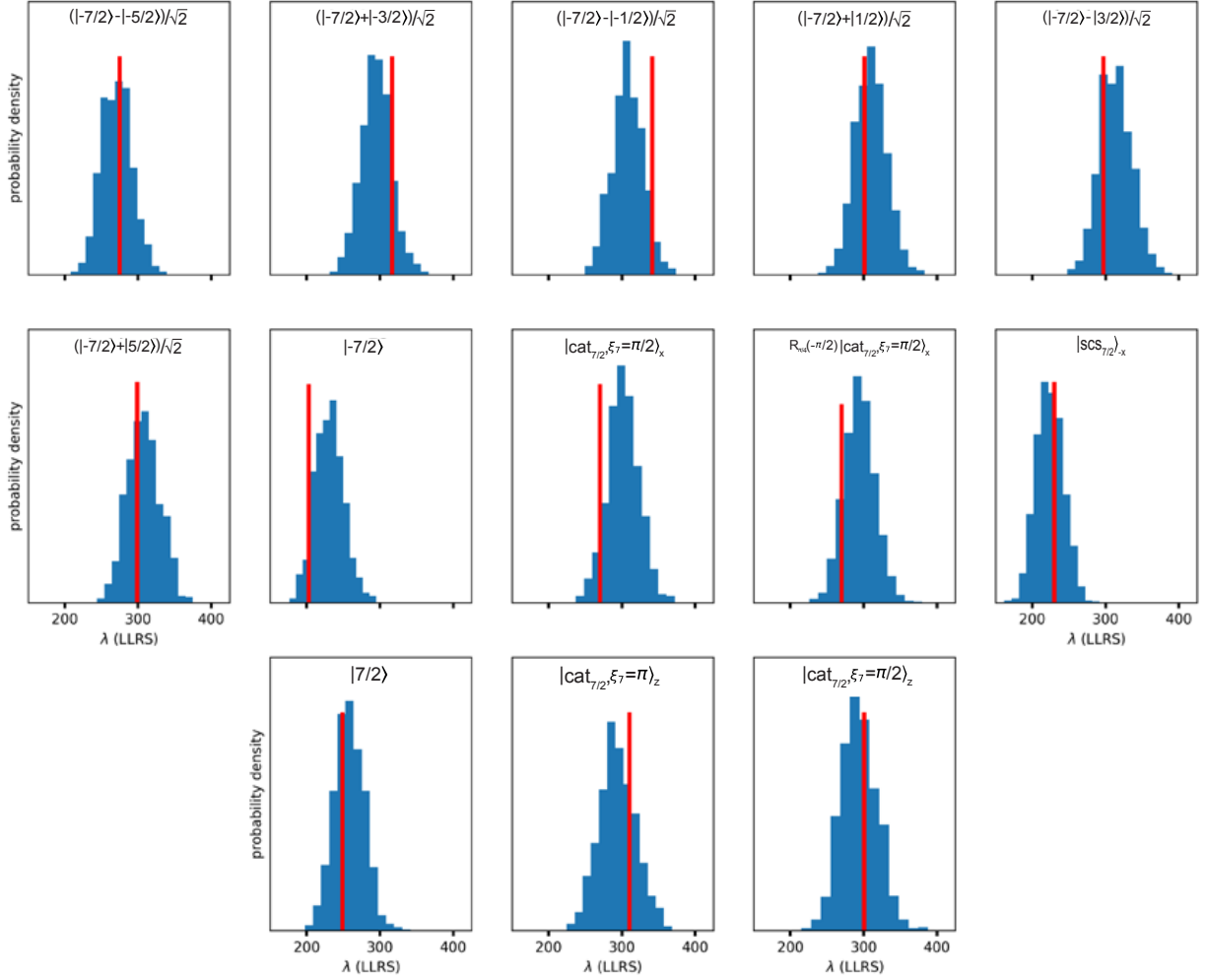


FIG. S13. Validation of tomographic state reconstructions. To check for possible errors or corruption in the measurement axes, a.k.a. *model violation*, we computed the loglikelihood ratio statistic (λ , see text for details) between the MLE state ρ_{MLE} and a saturated model. For each of the 13 states reconstructed, we used a parametric bootstrap to generate 1000 samples from the null distribution of λ (blue histogram) and compared the experimental λ (red) to it. No inconsistency was observed. The total runtime for computing the 24,000 MLEs needed by this procedure was under one hour.

C. Confirming the validity of the state tomography

State tomography has known weaknesses, because it relies on knowing exactly what measurements were performed. If the measurements actually performed in the experiment were noisy, flawed, or otherwise different from the mathematical models $\{E_n\}$ used in the MLE reconstruction, then the estimate ρ_{MLE} will be systematically wrong. We sought to rule out as many potential causes of systematic mis-estimation as possible.

First, we consider the possibility that we might have been performing *noisy* measurements, whose effects $\{E_n\}$ are not rank-1 projectors. Although this cannot be ruled out, we can say that its impact is small. We modeled our measurement effects as perfect rank-1 projectors. Additional noise in all the measurements would look the same as noise in the state, and would cause ρ_{MLE} to look more mixed (less pure). We do *not* observe this – our estimated states always have low rank, and are nearly pure. This certifies that our measurement effects are indeed close to rank-1.

Second, we consider the possibility that the measurement axes might be systematically rotated by some $SU(2)$ unitary. This also cannot be ruled out. However, it is also entirely inconsequential. Our main results are about the creation of “Schrödinger’s Cat” states that are highly delocalised over the sphere, and those properties are invariant under $SU(2)$ rotations. So systematic rotations of the measurement axes have no effect on our results.

Finally, we consider the possibility that *some* measurement axes might be erroneously rotated relative to the rest. This is the most interesting possibility. If the relative orientation of the measurement axes were to be corrupted in this

Target State	Method of Creation	Fidelity
$ -7/2 \rangle$	Initial state	0.990(1)
$ \text{scs}_{7/2} \rangle_x$	CR	0.934(3)
$ 7/2 \rangle$	CR	0.890(3)
$(-7/2 \rangle - -5/2 \rangle)/\sqrt{2}$	Given rotations	0.909(2)
$(-7/2 \rangle + -3/2 \rangle)/\sqrt{2}$	Given rotations	0.819(4)
$(-7/2 \rangle - -1/2 \rangle)/\sqrt{2}$	Given rotations	0.847(3)
$(-7/2 \rangle + 1/2 \rangle)/\sqrt{2}$	Given rotations	0.879(3)
$(-7/2 \rangle - 3/2 \rangle)/\sqrt{2}$	Given rotations	0.780(4)
$(-7/2 \rangle + 5/2 \rangle)/\sqrt{2}$	Given rotations	0.866(3)
$ \text{cat}_{7/2}, \xi_7 = \pi/2 \rangle_x$	CR + virtual-SNAP	0.883(4)
$R_{\pi/4}(-\pi/2) \text{cat}_{7/2}, \xi_7 = \pi/2 \rangle_x$	CR + virtual-SNAP	0.917(3)
$(-7/2 \rangle - 7/2 \rangle)/\sqrt{2}$	Givens rotations	0.794(2)
$(-7/2 \rangle + i 7/2 \rangle)/\sqrt{2}$	CR + virtual-SNAP	0.874(2)

TABLE S1. State fidelity, $\mathcal{F} = \langle \psi | \rho_{\text{MLE}} | \psi \rangle$, where ψ is the target state, and ρ_{MLE} is the density matrix obtained from maximum likelihood quantum state tomography.

way, it would cause inconsistency within the dataset [40, 41]. We can test for this using a loglikelihood ratio test [42] that compares the loglikelihood (a measure of goodness-of-fit) of the MLE density matrix ρ_{MLE} to a *saturated model* that is allowed to fit every measurement independently [43]. In the absence of any measurement-axis inconsistencies, the *null distribution* of the loglikelihood ratio statistic,

$$\lambda = -2 \log \left(\frac{\mathcal{L}(\rho_{\text{MLE}})}{\mathcal{L}_{\text{saturated}}} \right) \quad (67)$$

can be computed. Under ideal conditions, λ would behave as a χ^2_k random variable with $k = 315 - 63 = 252$ degrees of freedom, because the maximal model has 315 degrees of freedom and the density matrix has 63. However, positivity constraints on ρ complicate this picture [44]. Therefore, we used a parametric bootstrap (1000 samples) to evaluate the null distribution of λ for each of the 24 states we reconstructed. Then, we computed the experimental value of λ for each state, and compared them. The results are shown in Fig. S13. For each state, the observed λ is consistent with the null distribution, meaning that there is *no* evidence for any significant errors in the measurements.

In summary, we used the most powerful available statistical tools to search for evidence of inconsistencies in our tomography, and found none.

SI: 10. T_2^* FOR ADJACENT NUCLEAR SPIN LEVELS

We have repeated on this device an experiment reported earlier in Ref. [45], where we measured the nuclear dephasing times T_2^* by Ramsey experiments involving adjacent nuclear levels, i.e. by creating superpositions of the form $(|m_I\rangle + |m_I - 1\rangle)/\sqrt{2}$. We found again the expected trend where $T_2^*(m_I \leftrightarrow m_I - 1)$ is maximum for the $|1/2\rangle \leftrightarrow |-1/2\rangle$ transition, since it is to first-order insensitive to fluctuations in the nuclear quadrupole splitting, which can be caused by electrical noise in the device. The value of $T_2^*(1/2 \leftrightarrow -1/2) = 167(60)$ ms is particularly high in this device, which could be the result of a fortunate absence of ^{29}Si nuclear spins in the immediate vicinity of the ^{123}Sb nucleus under study (see Section SI: 12 for counterexamples).

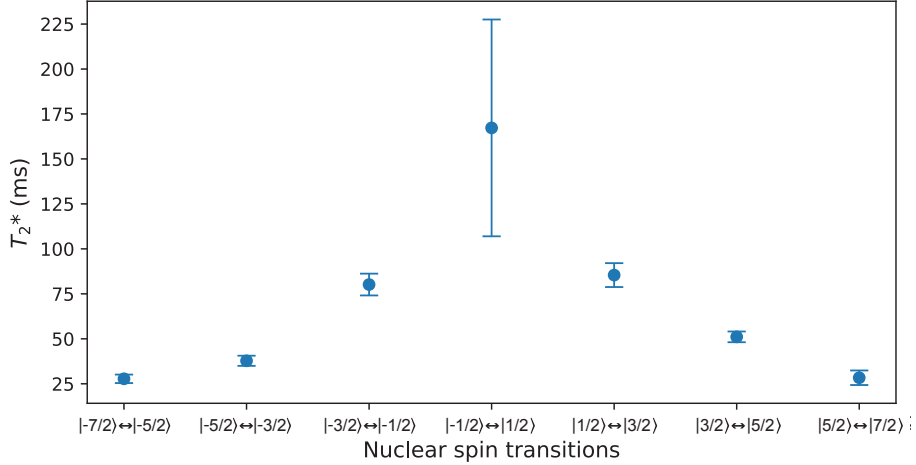


FIG. S14. **T_2^* for adjacent spin levels.** The value of T_2^* is extracted from fitting the Ramsey free induction decay, with each data point measured from the probabilities of spin states $|m_I - 1\rangle$ and $|m_I\rangle$ over 88 repetitions. The total experiment time of each Ramsey measurement is kept identical to ensure that the system experiences consistent temporal noise features.

SI: 11. NUCLEAR SPIN READOUT AND INITIALISATION

The initialisation and readout of the nuclear spin follows the methods described in [45, 46]. We summarise them again here for the readers' convenience, and to highlight the key features that affect the way we perform the experiments described in the main text.

Our experiments on creation and manipulation of Schrödinger cat states focus on using the ionised ^{123}Sb nuclear spin, i.e. the donor in the charge-positive D^+ state. However, reading out the nuclear spin populations requires introducing a hyperfine-coupled electron spin, which acts as a readout ancilla, as first demonstrated in the simpler ^{31}P system [47]. The electron is reintroduced on the donor by adjusting the voltages on the donor gates.

The Hamiltonian of the charge-neutral (D^0), coupled electron-nuclear system takes the form:

$$\hat{\mathcal{H}}_{D^0} = \gamma_e B_0 \hat{S}_z - \gamma_n B_0 \hat{I}_z + A \cdot \hat{\mathbf{S}} \cdot \hat{\mathbf{I}} + \hat{\mathcal{H}}_{Q^0}, \quad (68)$$

where $\gamma_e = 27.97$ GHz/T is the electron gyromagnetic ratio, $\gamma_n = 5.55$ MHz/T the nuclear gyromagnetic ratio, $\hat{\mathcal{H}}_{Q^0}$ the nuclear quadrupole interaction in the neutral donor (in general different from that in the ionised case), resulting in a typical quadrupole splitting $f_q^0 \sim 10\text{--}100$ kHz [45], and A is the Fermi contact hyperfine coupling, which in this specific donor takes the value $A \approx 98$ MHz. The hierarchy of energy scales $\gamma_e B_0 \approx 39$ GHz $\gg A \approx 98$ MHz $\gg f_q^0 \approx 100$ kHz ensures that the eigenstates of this Hamiltonian are to a good approximation the simple tensor products of the electron spin states $\{| \downarrow \rangle, | \uparrow \rangle\}$ and the nuclear projections $\{|m_I\rangle\}$.

Under these conditions, the electron exhibits 8 electron spin resonance (ESR) frequencies $f_{m_I}^{\text{ESR}}$, separated by $\approx A$, dependent on the state of the nucleus. Starting from the electron $|\downarrow\rangle$, an adiabatic frequency sweep [48] around each of the $f_{m_I}^{\text{ESR}}$ inverts the electron to the $|\uparrow\rangle$ state if the nucleus is in the state $|m_I\rangle$, i.e. performs a conditional quantum operation on the electron spin ancilla. The measurement is, to a good approximation, of quantum nondemolition (QND) nature [47, 49] (see Section SI: 11B for deviations from QND), and can be repeated multiple times to increase the readout fidelity. Here we use 8 repetitions of the cycle [load $|\downarrow\rangle$ – adiabatic ESR sweep around $f_{m_I}^{\text{ESR}}$ – measure electron state] for every nuclear orientation m_I . Because we are measuring a single nucleus, the electron spin responds

at only 1 of the 8 possible resonances, as shown in Fig. S15. Once the nuclear spin state $|m_I\rangle$ is determined, initialisation to other nuclear spin eigenstates can be achieved by using NMR π -pulses.

After preparing specific nuclear spin states, e.g. spin coherent state or cat states (Figs. 2, 3 and 4 of the main manuscript), the populations of each of the $|m_I\rangle$ states are extracted by repeating the preparation and nuclear readout cycles typically 100 times.

The electron spin readout and initialisation follows the standard method based on spin-dependent tunnelling [50, 51], whereby the electron can tunnel out of the donor if in the $|\uparrow\rangle$ state, whereas it remains bound to the donor if in the $|\downarrow\rangle$. The readout process automatically resets the electron spin in the $|\downarrow\rangle$ state. The method relies upon having a charge reservoir at very low temperature T , such that $\gamma_e B_0 \gg k_B T/h$, where k_B is the Boltzmann constant and h is the Planck constant. The electron readout is, in fact, the only aspect of our experiment that demands operation at millikelvin temperatures. Here, the cold charge reservoir is embodied by the island of a single-electron transistor (SET), which also acts as the charge detector that signals the electron tunnelling event in real-time [51].

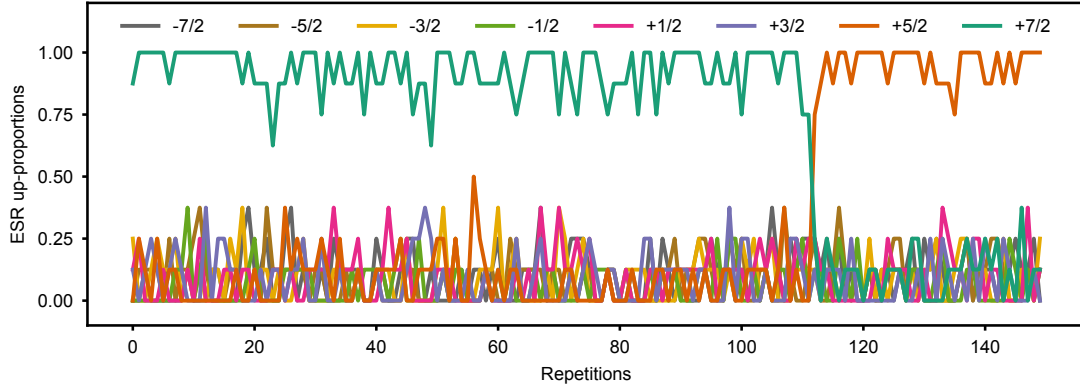


FIG. S15. Nuclear spin state readout. The ESR frequency depends on the state of the nuclear spin, and hence the nuclear spin state can be determined by sequentially pulsing 8 ESR transitions. Each nuclear spin state is read by 8 single-shot adiabatic inversions and electron-spin readout measurements. At the optimal readout point, only one of the eight ESR resonances exhibits notably high electron spin-up probabilities. The nuclear spin state is then identified as the one that conditions the electron resonance with the highest up-proportion.

A. Electron initialisation via a Maxwell's demon

When using spin-dependent tunnelling for electron spin readout and initialisation [50, 51], the fidelity is inherently limited by the thermal broadening of the Fermi distribution in the charge reservoir [52, 53]. The thermal limit to the fidelity of the $|\downarrow\rangle$ initialisation can be overcome by implementing a ‘Bayesian Maxwell’s demon’ [54]. This involves continuously monitoring the charge state of the donor and accepting it as $|\downarrow\rangle$ only after a stretch of time with no tunnelling events greatly exceeding the typical tunnel-out time of a $|\uparrow\rangle$ electron. If a tunnelling event does occur, the timer restarts and the process loops until it succeeds, at which the $|\downarrow\rangle$ is captured by lowering its electrochemical potential. In this device, we accept a $|\downarrow\rangle$ electron when the timer is able to reach 5 ms.

To assess the effectiveness of the Maxwell’s demon initialisation we perform NMR Rabi oscillations while the donor is in its neutral state. We drive the NMR pulse on-resonance with the transition between the states $| -7/2, \downarrow \rangle$ and $| -5/2, \downarrow \rangle$. Due to the hyperfine interaction, the resonance frequencies of the neutral NMR depend on the state of the electron [47]. If a $|\uparrow\rangle$ electron is loaded onto the donor, an NMR pulse tuned to flip the nucleus when the electron is $|\downarrow\rangle$ will be completely off-resonance and leave the nucleus unaffected. Therefore, the contrast of the neutral-donor nuclear spin Rabi oscillation is a direct measure of the electron $|\downarrow\rangle$ initialisation fidelity. In Fig. S16 b, we demonstrate that the adoption of the Bayesian Maxwell’s demon increases the contrast from 0.68(2) to 0.87(1), which corresponds to reducing the $|\downarrow\rangle$ initialisation error by a factor ≈ 2.5 .

B. Nuclear quantum jumps - deviation from QND nuclear readout

The energy relaxation time T_1 for nuclear spins in silicon is intrinsically very long, to be point of becoming immeasurable at cryogenic temperatures [55, 56], at least for the spin-1/2 ^{31}P nucleus. As an initial confirmation that T_1

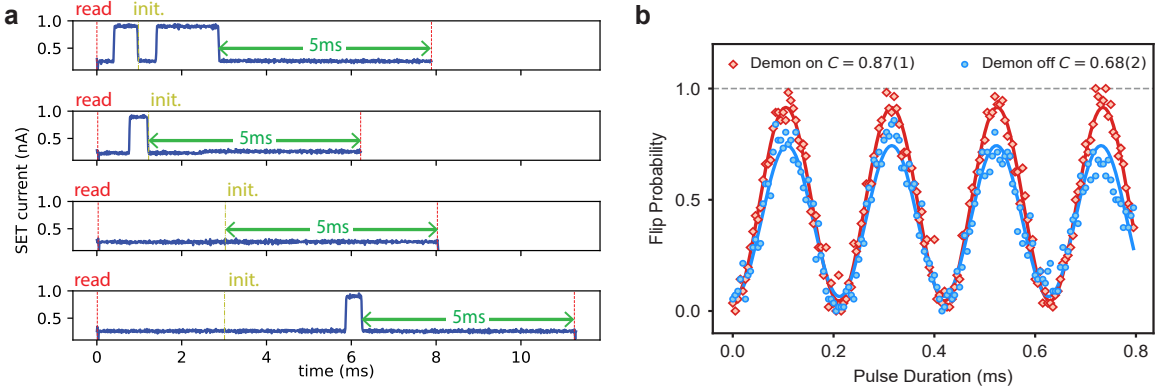


FIG. S16. **Electron spin initialisation with Bayesian Maxwell's demon.** **a**, real-time traces of the SET current during the readout and initialisation stages. We allow a readout window of at most 3 ms to detect the tunnel-out event of an electron spin-up state $|\uparrow\rangle$, signalled by the current suddenly jumping to a high value. The initialisation stage starts immediately after another electron tunnels back to the donor (top two panels), switching the current back to a low value. If no tunnelling event is registered within the 3 ms readout window (bottom two panels), the initialisation stage starts automatically. During the initialisation stage, an FPGA-based processor acts as the “Demon”, continuously monitoring tunnel-out events and cycling the process until no tunnel-out events are observed within a $t_{\text{init}} = 5$ ms window. **b**, Contrast of the neutral NMR Rabi oscillation when using (“Demon on”) or not using (“Demon off”) the Bayesian Maxwell’s demon to initialise the electron spin. Here, each nuclear flip probability is measured over 60 repetitions.

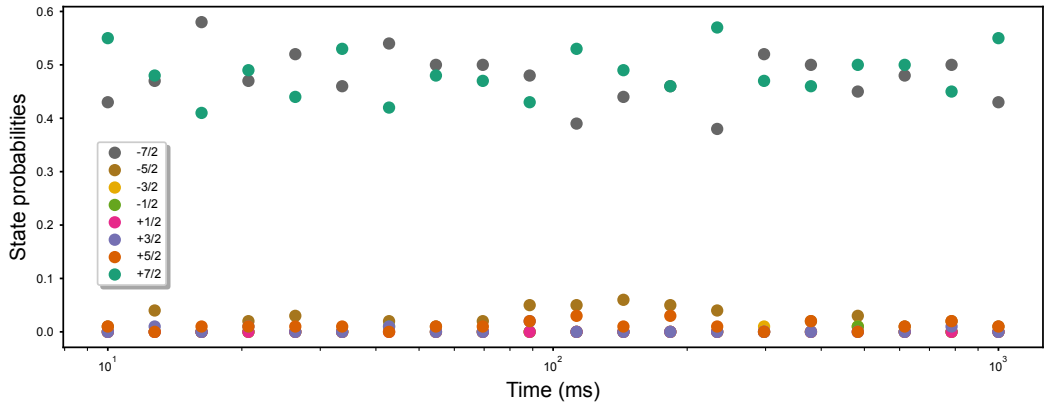


FIG. S17. Nuclear spin populations for a z -oriented cat state, measured after introducing a variable wait time up to 1 second. The absence of e.g. a decay in the $\pm 7/2$ populations indicates that the intrinsic T_1 is much longer than the maximum wait time adopted here. The probabilities of all 8 nuclear spin states are measured over 100 repetitions of nuclear projection measurements (see Section SI: 11).

is very long also in ^{123}Sb , we measured the state populations of a $|\text{cat}_{7/2}\rangle_z$ state after a wait time of up to 1 second (Fig. S17). The data shows no clear trend of population change as a function of wait time, suggesting that T_1 is likely to be $\gg 10$ s, possibly orders of magnitude more.

Therefore, the only mechanism to affect the nuclear spin populations is the measurement, which requires the repetitive loading and unloading of the donor electron (Section SI: 4C). The system Hamiltonian thus suddenly switches between $\hat{\mathcal{H}}_{D+}$ (See Eq. (1) in the main text) and $\hat{\mathcal{H}}_{D^0}$, where the latter includes the hyperfine interaction term $A \cdot \hat{\mathbf{S}} \cdot \hat{\mathbf{i}}$, and potentially a different quadrupole term $\hat{\mathcal{H}}_{Q^0}$. The slight change in the exact nuclear eigenstates between the two Hamiltonians introduces the possibility of ‘quantum jumps’ [47], which can be viewed as the consequence of the measurement not being exactly QND [49]. The process whereby electron tunnelling causes nuclear spin flips is sometimes called ‘ionisation shock’ [57]. In our system, this process constitutes effectively the main source of state preparation and measurement (SPAM) error.

We measure the susceptibility of each nuclear eigenstate $|m_I\rangle$ to ionisation shock by performing repeated nuclear readouts on the state, and plotting the typical length of sequences where no spin flips occur (Fig. S18). We observe a clear trend where states with lower $|m_I|$, i.e. close to the equator of the spin- $7/2$ Bloch sphere, display a higher

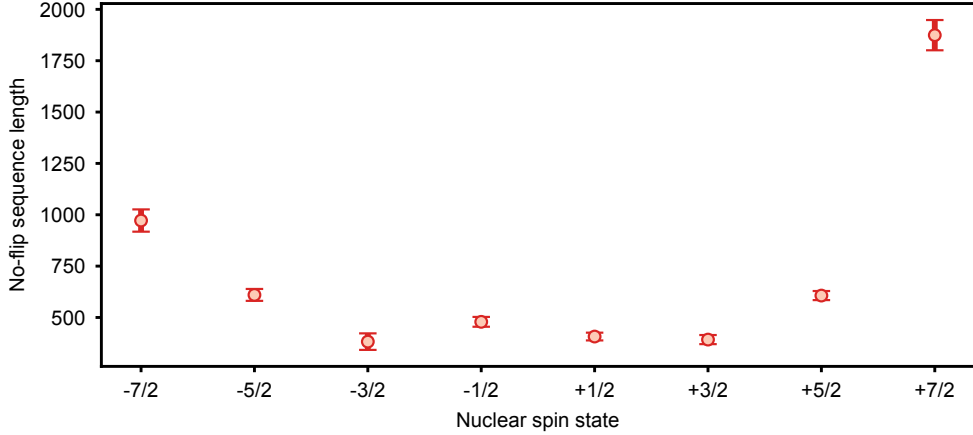


FIG. S18. Nuclear quantum jumps caused by ionisation shock. For each nuclear spin state $|7/2, m_I\rangle$, we repeat single-shot readout of the electron with an ESR pulse at the frequency of $f_{m_I}^{\text{ESR}}$ until 5 consecutive failure detections of electron spin-up $|\uparrow\rangle$ occur. Upon such an event, the nuclear jump event is registered, following which we initialise the nuclear state back to $|7/2, m_I\rangle$ by NMR pulse. This process is repeated 1000 times. Each "no-flip sequence length" value is obtained from fitting an exponential decay to a histogram of the occurrence of sequences without quantum jumps against the sequence length.

probability of quantum jumps. A detailed model of this trend is left to future work.

SI: 12. OTHER DEVICES

For this project, we fabricated a batch of ^{123}Sb -implanted devices, three of which were measured in a dilution refrigerator. We label the devices 'A' (the one used for all data shown in this paper), 'B' and 'C'. Devices A and C were produced with the same ^{123}Sb implantation parameters (18 keV acceleration energy, $5 \times 10^{11} \text{ cm}^{-2}$ fluence), while device B was produced with different ^{123}Sb implantation parameters (10 keV, $4 \times 10^{11} \text{ cm}^{-2}$). All other aspects of devices A-C are nominally identical. Fig. S19 shows the NMR spectra, covariant $SU(2)$ rotations and parity oscillations performed on these devices. The NMR spectra of the three different devices, shown in Fig. S19a-c, show a wide range of values for the quadrupole splitting f_q^+ , where even the sign can vary from device to device. The sign and magnitude of f_q^+ depends on the orientation of the applied magnetic field B_0 with respect to the principal axes of the electric field gradient at the nucleus. [46, 58]. In Device C, this conjures a value of $f_q^+ = -3.6 \text{ kHz}$ (Fig. S19c, device C), which complicates the execution of even simple Givens rotations or covariant $SU(2)$ rotations due to the low power necessary to resolve individual transitions. It is possible that a different magnetic field orientation could increase f_q^+ in Device C to a workable range, but this experiment was not attempted. Device C was therefore not subjected to further studies. On Device B, we proceeded to perform $SU(2)$ covariant rotations and create Schrödinger cat states with parity oscillations comparable to those of Device A, showing the general robustness of our methods.

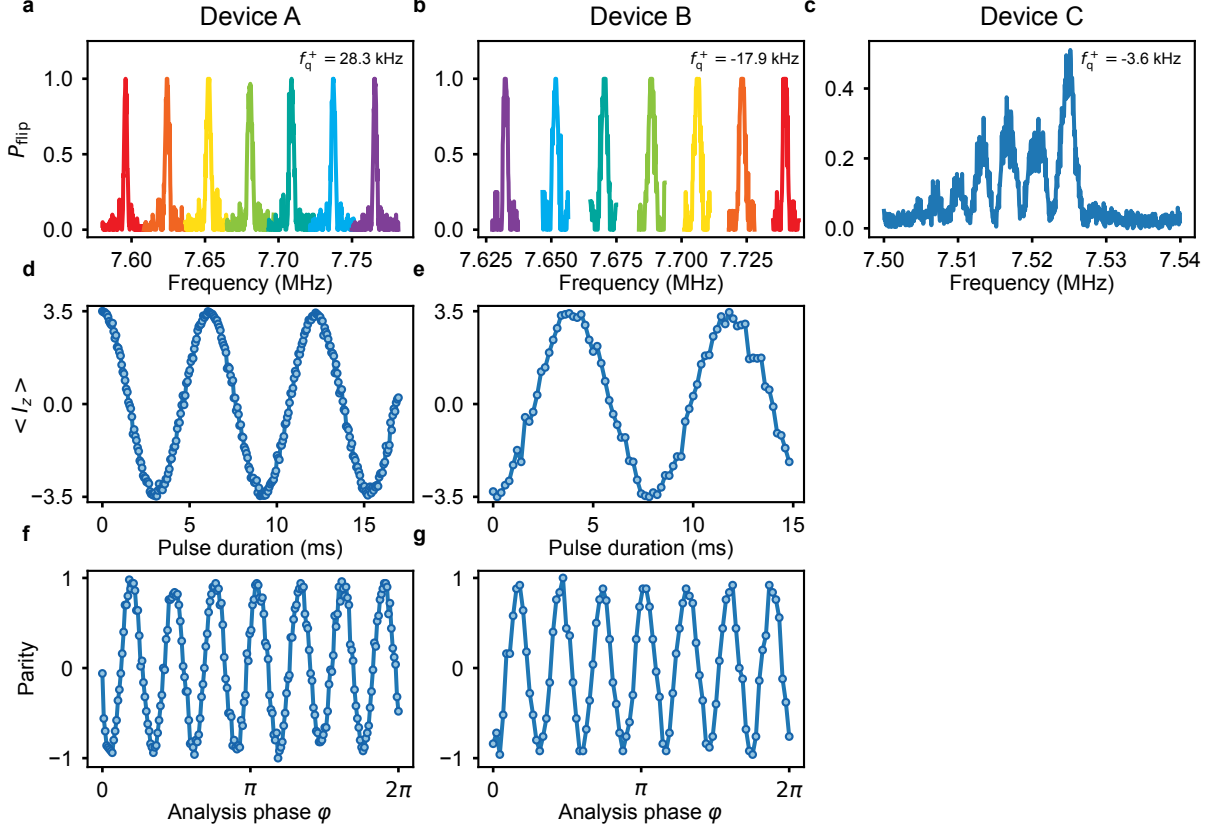


FIG. S19. NMR spectra, covariant $SU(2)$ rotations and parity oscillations in other devices. **a-c**, NMR spectra displaying the 7 NMR transitions of the ^{123}Sb nucleus. The spacing between the peaks indicates the quadrupole splitting f_q^+ , as denoted in the plot. Different colors represent different datasets, where the color labelling is consistent with Fig. 1 of the main text (i.e. red represents f_1 , purple f_7). In **a-b**, measurements are performed after initialisation in one of the nuclear spin states involved in the respective NMR transition. In **c**, the NMR spectrum is a single dataset without nuclear state initialisation, hence the irregular peak heights. **d-e**, Covariant $SU(2)$ rotations on devices A and B. Device B shows a significant decay in the covariant $SU(2)$ rotation shown in panel **e**. **f-g**, Parity oscillations of a $|\text{cat}_{7/2}\rangle_z$ state for devices A and B. Due to operational limitations caused by the small quadrupole splitting in device C, no covariant $SU(2)$ rotations and parity oscillations were performed for that device.

-
- [1] Radcliffe, J. M. Some properties of coherent spin states. *Journal of Physics A: General Physics* **4**, 313–323 (1971).
- [2] Gazeau, J.-P. *Coherent States in Quantum Physics* (Wiley, 2009), 1 edn.
- [3] Mourik, V. *et al.* Exploring quantum chaos with a single nuclear spin. *Physical Review E* **98**, 042206 (2018).
- [4] Goldberg, A. Z., Klimov, A. B., Grassl, M., Leuchs, G. & Sánchez-Soto, L. L. Extremal quantum states. *AVS Quantum Science* **2**, 044701 (2020).
- [5] Refs. [2],[4] use J , S , respectively for the spin quantum number that we refer to as I instead.
- [6] Hudson, R. When is the wigner quasi-probability density non-negative? *Reports on Mathematical Physics* **6**, 249–252 (1974).
- [7] DasGupta, A. Disentanglement formulas: An alternative derivation and some applications to squeezed coherent states. *American Journal of Physics* **64**, 1422–1427 (1996).
- [8] Heiss, S. & Weigert, S. Discrete moyan-type representations for a spin. *Physical Review A* **63** (2000).
- [9] Davis, J., Kumari, M., Mann, R. B. & Ghose, S. Wigner negativity in spin-j systems. *Physical Review Research* **3**, 033134 (2021).
- [10] Technically, the negativity also requires overlapping support of the Wigner functions for the two SCS, but this is already true in this case.

- [11] Agarwal, G. S. Relation between atomic coherent-state representation, state multipoles, and generalized phase-space distributions. *Physical Review A* **24**, 2889–2896 (1981).
- [12] Johansson, J., Nation, P. & Nori, F. Qutip: An open-source python framework for the dynamics of open quantum systems. *Computer Physics Communications* **183**, 1760–1772 (2012).
- [13] Johansson, J., Nation, P. & Nori, F. Qutip 2: A python framework for the dynamics of open quantum systems. *Computer Physics Communications* **184**, 1234–1240 (2013).
- [14] Cai, W., Ma, Y., Wang, W., Zou, C.-L. & Sun, L. Bosonic quantum error correction codes in superconducting quantum circuits. *Fundamental Research* **1**, 50–67 (2021).
- [15] Cochrane, P. T., Milburn, G. J. & Munro, W. J. Macroscopically distinct quantum-superposition states as a bosonic code for amplitude damping. *Physical Review A* **59**, 2631–2634 (1999).
- [16] Biedenharn, L. C. & Louck, J. D. *Angular Momentum in Quantum Physics: Theory and Application*. Encyclopedia of Mathematics and its Applications (Cambridge University Press, 1984).
- [17] Muhonen, J. T. *et al.* Storing quantum information for 30 seconds in a nanoelectronic device. *Nature Nanotechnology* **9**, 986–991 (2014).
- [18] Giacomini, F., Castro-Ruiz, E. & Brukner, Č. Quantum mechanics and the covariance of physical laws in quantum reference frames. *Nature Communications* **10**, 494 (2019).
- [19] Leuenberger, M. N. & Loss, D. Grover algorithm for large nuclear spins in semiconductors. *Physical Review B* **68**, 165317 (2003).
- [20] Dehollain, J. *et al.* Nanoscale broadband transmission lines for spin qubit control. *Nanotechnology* **24**, 015202 (2012).
- [21] Johansson, J., Nation, P. & Nori, F. Qutip 2: A python framework for the dynamics of open quantum systems. *Computer Physics Communications* **184**, 1234–1240 (2013).
- [22] McCoy, M. A. & Warren, W. S. Pulse shaping in quadrupole-echo NMR. *Journal of Magnetic Resonance (1969)* **98**, 24–35 (1992).
- [23] Brennen, G. K., O’Leary, D. P. & Bullock, S. S. Criteria for exact qudit universality. *Phys. Rev. A* **71**, 052318 (2005).
- [24] Spengler, C., Huber, M. & Hiesmayr, B. C. A composite parameterization of unitary groups, density matrices and subspaces. *Journal of Physics A Mathematical General* **43**, 385306 (2010). 1004.5252.
- [25] Krastanov, S. *et al.* Universal control of an oscillator with dispersive coupling to a qubit. *Physical Review A* **92**, 040303 (2015).
- [26] Heeres, R. W. *et al.* Cavity state manipulation using photon-number selective phase gates. *Physical Review Letters* **115**, 137002 (2015).
- [27] Sawicki, A. & Karnas, K. Universality of single-qudit gates. *Annales Henri Poincaré* **18**, 3515–3552 (2017).
- [28] Kitagawa, M. & Ueda, M. Squeezed spin states. *Physical Review A* **47**, 5138–5143 (1993).
- [29] Gupta, P., Vaartjes, A., Yu, X., Morello, A. & Sanders, B. C. Robust macroscopic Schrödinger’s cat on a nucleus. *Physical Review Research* **6**, 013101 (2024).
- [30] Davis, J., Hennigar, R. A., Mann, R. B. & Ghose, S. Stellar representation of extremal wigner-negative spin states. *Journal of Physics A: Mathematical and Theoretical* **56**, 265302 (2023).
- [31] Turchette, Q. A. *et al.* Deterministic entanglement of two trapped ions. *Physical Review Letters* **81**, 3631–3634 (1998).
- [32] Chen, B. *et al.* Quantum state tomography of a single electron spin in diamond with wigner function reconstruction. *Applied Physics Letters* **114** (2019).
- [33] Hradil, Z. Quantum-state estimation. *Physical Review A* **55**, R1561 (1997).
- [34] Hofmann, H. F. & Takeuchi, S. Quantum-state tomography for spin-1 systems. *Physical Review A* **69**, 042108 (2004).
- [35] Newton, R. G. & Young, B.-L. Measurability of the spin density matrix. *Annals of Physics* **49**, 393–402 (1968).
- [36] Perlin, M. A., Barberena, D. & Rey, A. M. Spin qudit tomography and state reconstruction error. *Physical Review A* **104**, 062413 (2021).
- [37] Renes, J. M., Blume-Kohout, R., Scott, A. J. & Caves, C. M. Symmetric informationally complete quantum measurements. *Journal of Mathematical Physics* **45**, 2171–2180 (2004).
- [38] Agrawal, A., Verschueren, R., Diamond, S. & Boyd, S. A rewriting system for convex optimization problems. *Journal of Control and Decision* **5**, 42–60 (2018).
- [39] Dahl, J. & Andersen, E. D. A primal-dual interior-point algorithm for nonsymmetric exponential-cone optimization. *Mathematical Programming* **194**, 341–370 (2021).
- [40] Shulman, M. D. *et al.* Demonstration of entanglement of electrostatically coupled singlet-triplet qubits. *Science* **336**, 202–205 (2012).
- [41] van Enk, S. J. & Blume-Kohout, R. When quantum tomography goes wrong: Drift of quantum sources and other errors. *New Journal of Physics* **15**, 025024 (2013).
- [42] Blume-Kohout, R., Yin, J. O. & van Enk, S. Entanglement verification with finite data. *Physical Review Letters* **105**, 170501 (2010).
- [43] Nielsen, E. *et al.* Gate set tomography. *Quantum* **5**, 557 (2021).
- [44] Scholten, T. L. & Blume-Kohout, R. Behavior of the maximum likelihood in quantum state tomography. *New Journal of Physics* **20**, 023050 (2018).
- [45] Fernández de Fuentes, I. *et al.* Navigating the 16-dimensional Hilbert space of a high-spin donor qudit with electric and magnetic fields. *Nature Communications* **15**, 1380 (2024).
- [46] Asaad, S. *et al.* Coherent electrical control of a single high-spin nucleus in silicon. *Nature* **579**, 205–209 (2020).
- [47] Pla, J. J. *et al.* High-fidelity readout and control of a nuclear spin qubit in silicon. *Nature* **496**, 334–338 (2013).
- [48] Laucht, A. *et al.* High-fidelity adiabatic inversion of a ^{31}P electron spin qubit in natural silicon. *Applied Physics Letters*

- 104, 092115 (2014).
- [49] Joecker, B., Stemp, H. G., de Fuentes, I. F., Johnson, M. A. & Morello, A. Error channels in quantum nondemolition measurements on spin systems. *Physical Review B* **109**, 085302 (2024).
 - [50] Elzerman, J. M. *et al.* Single-shot read-out of an individual electron spin in a quantum dot. *Nature* **430**, 431–435 (2004).
 - [51] Morello, A. *et al.* Single-shot readout of an electron spin in silicon. *Nature* **467**, 687–691 (2010).
 - [52] Beenakker, C. W. J. Theory of Coulomb-blockade oscillations in the conductance of a quantum dot. *Physical Review B* **44**, 1646–1656 (1991).
 - [53] van der Wiel, W. G. *et al.* Electron transport through double quantum dots. *Reviews of Modern Physics* **75**, 1–22 (2002).
 - [54] Johnson, M. A. *et al.* Beating the thermal limit of qubit initialization with a Bayesian Maxwell’s demon. *Physical Review X* **12**, 041008 (2022).
 - [55] Saeedi, K. *et al.* Room-temperature quantum bit storage exceeding 39 minutes using ionized donors in silicon-28. *Science* **342**, 830–833 (2013).
 - [56] Savitskyy, R. *et al.* An electrically driven single-atom “flip-flop” qubit. *Science Advances* **9**, eadd9408 (2023).
 - [57] Hile, S. J. *et al.* Addressable electron spin resonance using donors and donor molecules in silicon. *Science advances* **4**, eaqq1459 (2018).
 - [58] Franke, D. P. *et al.* Interaction of strain and nuclear spins in silicon: Quadrupolar effects on ionized donors. *Physical Review Letters* **115**, 057601 (2015).